Article

Molecular Cell

Histone Ubiquitination by the DNA Damage Response Is Required for Efficient DNA Replication in Unperturbed S Phase

Graphical Abstract

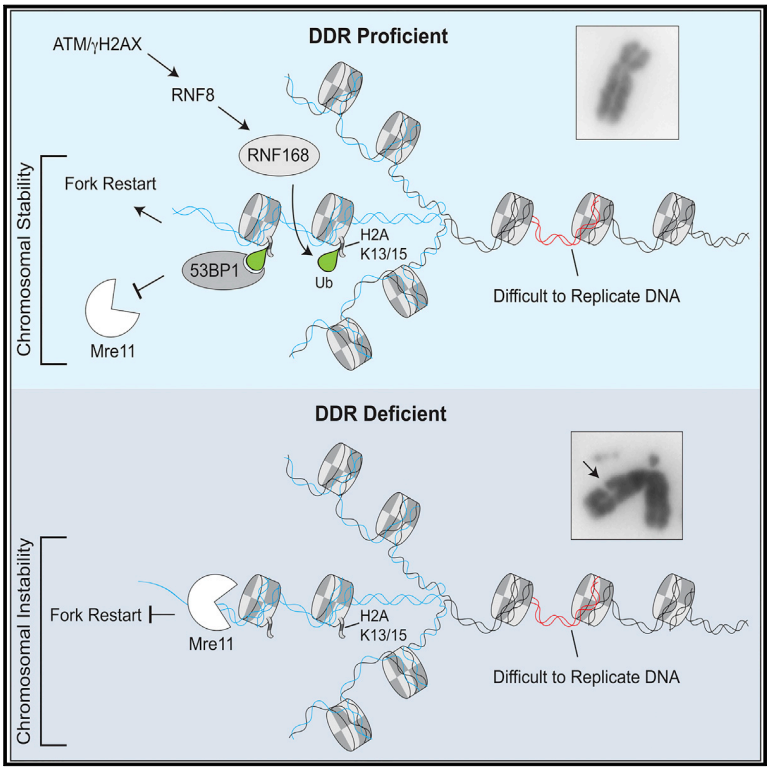

Highlights

- Canonical DDR factors mediate efficient fork progression during unperturbed S phase
- DDR factors limit reversed fork accumulation and processing at repetitive DNA
- H2A K13/K15 ubiquitination by RNF168 is required for efficient fork progression
- The regressed arms of reversed forks are regularly chromatinized

Authors

Jonas Andreas Schmid, Matteo Berti, Franziska Walser, ..., Raimundo Freire, Massimo Lopes, Lorenza Penengo

Correspondence

lopes@imcr.uzh.ch (M.L.), penengo@imcr.uzh.ch (L.P.)

In Brief

Genome duplication during cell proliferation is an endogenous source of genotoxic stress. Schmid et al. find that DNA damage response (DDR) factors—so far implicated in chromosomal break repair—are essential to modulate remodeling and restart of transiently stalled forks during unperturbed S phase, suggesting alternative DDR roles in genome maintenance.

Schmid et al., 2018, Molecular Cell *71*, 897–910
September 20, 2018
https://doi.org/10.1016/j.molcel.2018.07.011

CellPress

Molecular Cell
Article

Histone Ubiquitination by the DNA Damage Response Is Required for Efficient DNA Replication in Unperturbed S Phase

Jonas Andreas Schmid,[1] Matteo Berti,[1] Franziska Walser,[1] Maria Chiara Raso,[1] Fabian Schmid,[1] Jana Krietsch,[1] Henriette Stoy,[1] Katharina Zwicky,[1] Sebastian Ursich,[1] Raimundo Freire,[2] Massimo Lopes,[1,*] and Lorenza Penengo[1,3,*]
[1]Institute of Molecular Cancer Research, University of Zurich, Zurich 8057, Switzerland
[2]Unidad de Investigación, Hospital Universitario de Canarias, Instituto de Tecnologías Biomédicas, Ofra s/n, La Cuesta, La Laguna, Tenerife 38320, Spain
[3]Lead Contact
*Correspondence: lopes@imcr.uzh.ch (M.L.), penengo@imcr.uzh.ch (L.P.)
https://doi.org/10.1016/j.molcel.2018.07.011

SUMMARY

Chromatin ubiquitination by the ubiquitin ligase RNF168 is critical to regulate the DNA damage response (DDR). DDR deficiencies lead to cancer-prone syndromes, but whether this reflects DNA repair defects is still elusive. We identified key factors of the RNF168 pathway as essential mediators of efficient DNA replication in unperturbed S phase. We found that loss of RNF168 leads to reduced replication fork progression and to reversed fork accumulation, particularly evident at repetitive sequences stalling replication. Slow fork progression depends on MRE11-dependent degradation of reversed forks, implicating RNF168 in reversed fork protection and restart. Consistent with regular nucleosomal organization of reversed forks, the replication function of RNF168 requires H2A ubiquitination. As this novel function is shared with the key DDR players ATM, γH2A.X, RNF8, and 53BP1, we propose that double-stranded ends at reversed forks engage classical DDR factors, suggesting an alternative function of this pathway in preventing genome instability and human disease.

INTRODUCTION

Maintenance of genome stability is an active process within the cells, which cope with the huge number of DNA lesions arising both from exogenous (i.e., genotoxic drugs and irradiation) and endogenous (i.e., DNA replication) sources. Ubiquitin (Ub)-mediated post-translational modifications play essential roles in this process, finely regulating both the DNA damage response (DDR) and DNA replication (Smeenk and Mailand, 2016). A paradigmatic example of the ubiquitination signaling role is represented by the pathway activated by DNA double-strand breaks (DSBs). Upon DSB formation, the histone variant H2A.X is phosphorylated by the ATM kinase, leading to the recruitment of the ubiquitinating pair RNF8/UBC13, which promotes K63-linked ubiquitination (Smeenk and Mailand, 2016). These ubiquitinating events allow the recruitment of the Ub ligase RNF168 to damaged chromosomes, where it targets histones H2A and H2A.X in a UbK27-dependent manner (Gatti et al., 2015). Remarkably, RNF168 generates a highly specific mark on chromatin by modifying the N-terminal site of H2As on K13 and K15 (Gatti et al., 2012; Mattiroli et al., 2012), referred to as H2AK13/15Ub. Ubiquitinated H2As represent the docking site for additional factors, such as 53BP1 and the BRCA1 complex, which activate downstream events to repair damaged DNA by promoting either non-homologous end joining (NHEJ) or homologous recombination (HR), respectively.

RNF168's activity and the H2AK13/15Ub histone mark are at the hub of the DDR pathway, and their key role has been clearly demonstrated by the identification of germline mutations in the *RNF168* gene as the cause of a combined disorder called RIDDLE syndrome, characterized by radiosensitivity, immunodeficiency, microcephaly, growth retardation, and cancer predisposition (Stewart et al., 2009). Similarly, mutations in the apical kinase ATM are associated with the human syndrome ataxia telangiectasia, which combines neurological defects with immunosuppression and elevated cancer risk. Knockout mouse models for all genes in this pathway are compatible with life but display different combinations of phenotypes, such as abnormal development, infertility, immunodeficiencies, premature aging, and/or cancer predisposition (Specks et al., 2015). Overall, while immunodeficiency and radiosensitivity are clearly linked to the DSB response defect, the molecular mechanisms underlying the other defects are currently unknown.

Recent work has investigated the role of classical DSB processing and signaling factors in response to replication stress. HR factors have long been known to mediate specialized pathways of replication fork restart, although this was long assumed to involve collapse of stalled forks into DSBs (Petermann and Helleday, 2010). Moreover, DSB processing factors—such as the MRE11 nuclease—were found to regulate ssDNA accumulation on replication intermediates (Hashimoto et al., 2010). The BRCA genes—key HR factors and tumor suppressors—were shown to limit this MRE11-dependent fork resection, preventing extensive degradation of newly synthesized DNA

(Schlacher et al., 2011). This alternative function of these crucial HR factors can be genetically uncoupled from their classical role in DSB repair and was recently reported to underlie the exquisite chemosensitivity observed in BRCA2-defective tumors (Ray Chaudhuri et al., 2016; Schlacher et al., 2011). Differently from DSB processing and repair, the relevance of the DSB signaling pathway in DNA replication has not yet been thoroughly investigated. Large 53BP1 foci in G1 phase—described as "53BP1 nuclear bodies" (Lukas et al., 2011)—arise as a consequence of increased replication stress in the previous S phase via mitotic processing of residual replication intermediates into DSBs. Recently, Rad9/53BP1 was shown in yeast to protect stalled forks from degradation (Villa et al., 2018) and to modulate in mammals checkpoint signaling and stalled fork restart (Her et al., 2018; Xu et al., 2017). However, these observations were made upon exogenous genotoxic treatments, and a potential role of DSB signaling factors in unperturbed replication has not been investigated to date.

Replication fork remodeling into four-way junctions—also known as replication fork reversal—has recently emerged as a global response to a variety of conditions of replication stress, including treatment with multiple genotoxins (Ray Chaudhuri et al., 2012; Zellweger et al., 2015). Intriguingly, repetitive sequences prone to form secondary structures are also sufficient to induce frequent fork reversal during unperturbed S phase (Follonier et al., 2013). This transaction was proposed to limit fork progression under unfavorable conditions, thereby preventing breakage of replicating chromosomes (Neelsen and Lopes, 2015). However, the regressed arm of reversed forks was also recently shown to act as a necessary entry point for fork degradation in BRCA-defective cells (Lemaçon et al., 2017; Mijic et al., 2017; Taglialatela et al., 2017). The striking structural similarity between the double-stranded end of regressed arms and DSBs raises the intriguing possibility that DSB processing as well as DSB signaling factors modulate stability and restart of transiently stalled forks while they are remodeled into four-way junctions.

Here we show that RNF168 and other factors of the DDR cascade are recruited to replication factories and promote efficient replication fork progression during unperturbed S phase by preventing reversed fork accumulation at difficult-to-replicate sequences and their processing by MRE11 nuclease. This alternative function of the DDR pathway requires RNF168-dependent ubiquitination of H2A, suggesting that modifications of chromatin—which we found regularly assembled on the regressed arms—promote efficient restart of endogenously formed reversed forks and allow continuous fork progression. This novel activity of the DDR pathway may provide alternative molecular explanations to the complex phenotypes associated with DDR defects in animal models and human cancer-prone syndromes.

RESULTS

RNF168 Localizes at Replication Factories in Unperturbed Conditions

Although RNF168 activity has been extensively studied in the context of DSB signaling, not much is known about its function during unperturbed proliferation. We thought to retrieve some information from its subcellular localization in undamaged cells: while RNF168 is rapidly recruited to DDR foci upon induction of DSBs, showing an evident punctuate staining, its distribution in unperturbed conditions is more heterogeneous within the cell population. However, using a U2OS Flp-In T-REx system expressing FLAG-RNF168 to obtain controlled and detectable expression of RNF168, we noted that in a subpopulation of cells undergoing DNA replication, RNF168 partially co-localizes with replication factories marked by PCNA foci (Figure 1A). We thus investigated a possible association between RNF168 and PCNA by performing co-immunoprecipitation and GST pull-down experiments. Both biochemical approaches suggest that PCNA and RNF168 interact in cells (Figure 1B). To further substantiate this observation, we set up a proximity ligation assay (PLA) between RNF168 and PCNA, using both wild-type FLAG-RNF168 and a mutant form (referred as UBD), which is unable to bind ubiquitinated proteins and hence does not properly localize to chromatin (Figure 1C) (Penengo et al., 2006; Pinato et al., 2011). PLA analysis shows that RNF168 can be found in close proximity to PCNA, while the UBD does not show any significant association (Figure 1D). Moreover, to determine whether RNF168/PCNA interaction occurs in a specific cell cycle phase, we labeled cells with 5-ethynyl-2′-deoxyuridine (EdU) to clearly mark DNA synthesis, and we analyzed them by quantitative image-based cytometry (QIBC) (Toledo et al 2013). This allowed us to determine that the interaction between RNF168 and PCNA, measured by PLA, mainly occurs during late S phase (Figures 1E, 1F, and S1). Using a similar experimental setting, we found that the cell cycle distribution of the histone modification H2AK15Ub, specifically generated by RNF168, correlates with the distribution of PLA signal obtained for RNF168/PCNA (Figures 1G and 1H), indicating that RNF168 is active on chromatin in this specific cell cycle phase. Together these data suggest a potential role of RNF168 in DNA replication during unperturbed S phase.

RNF168 Is Required for Proper DNA Replication in Unperturbed Conditions

To test this hypothesis, we asked whether depletion of RNF168 has an impact on DNA synthesis, by measuring EdU incorporation in S phase using flow cytometry. We found that U2OS shRNF168 cells show a marked reduction in the rate of EdU incorporation upon *RNF168* downregulation, indicating impaired DNA synthesis (Figures 2A, S1A, and S1B). We next used the DNA fiber spreading assay (Jackson and Pombo, 1998) to investigate the effect of RNF168 depletion on replication fork progression at single-molecule level. Strikingly, we found an approximately 40% reduction in fork speed in unperturbed RNF168-deficient cells, using either shRNA- or siRNA-mediated downregulation with different target sequences (Figure 2B). This reduction in fork speed involved the full population of replication forks and was also visible upon shorter labeling times, albeit less pronounced (Figure S2C). We next assessed whether this reduced fork speed reflected frequent fork pausing by analyzing forks diverging from the same replication origin. While in control cells these forks move at similar rates, RNF168 depletion led to marked sister fork asymmetry, indicating an increased frequency of fork stalling upon RNF168 inactivation (Figure 2C).

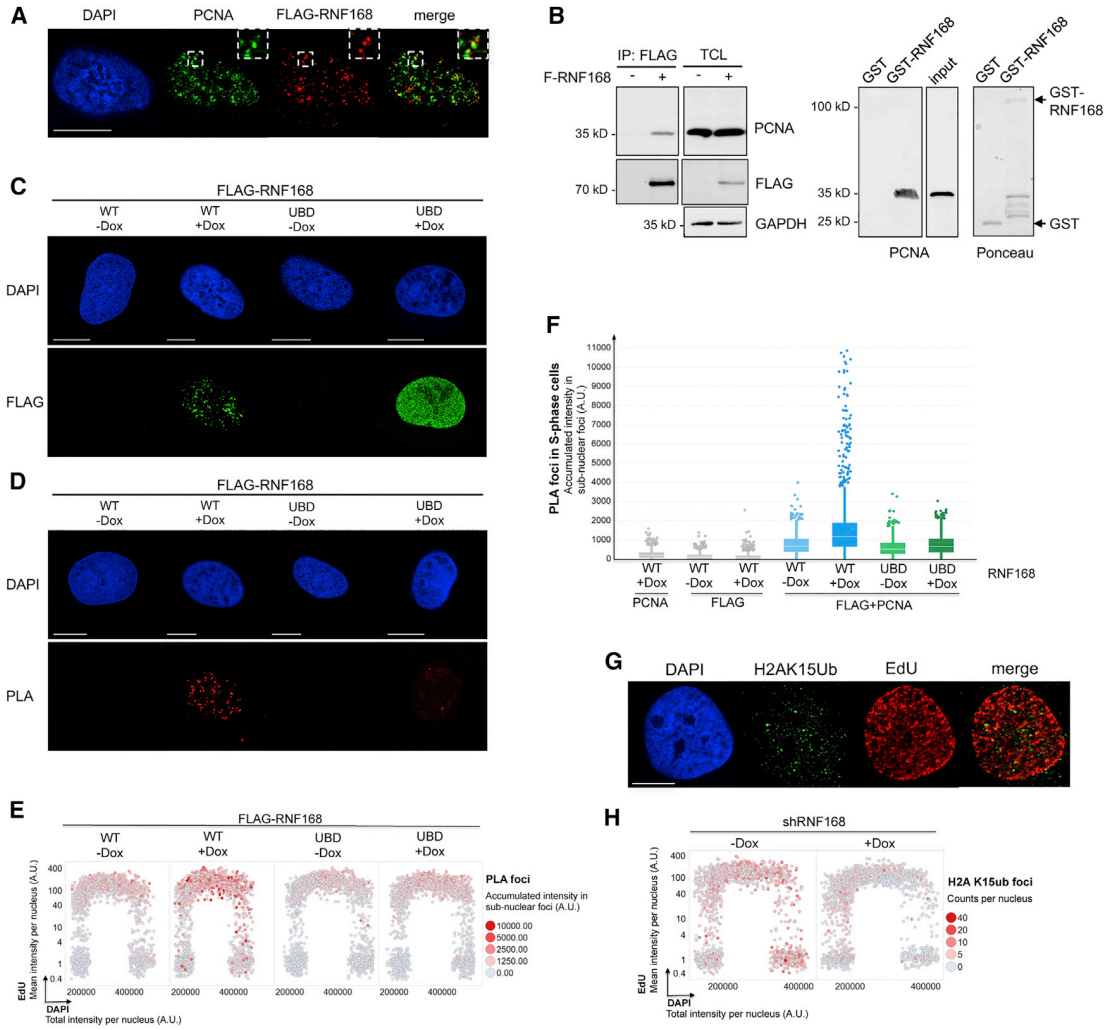

Figure 1. RNF168 Localizes at Replication Forks

(A) Representative images showing the partial co-localization of RNF168 and PCNA in U2OS Flp-In T-REx cells expressing doxycycline (Dox)-inducible FLAG-RNF168 for 24 hr.

(B) Immunoblots validating the interaction of RNF168 and PCNA by coIP (left) or GST pull-down (right).

(C) Expression of FLAG-RNF168 wild-type (WT) and ubiquitin binding-deficient RNF168 (UBD) in Dox-inducible U2OS Flp-In T-REx cell lines.

(D) Representative images showing the proximity ligation assay (PLA) signal between FLAG-RNF168 (WT and UBD) and PCNA.

(E) Quantification of PLA accumulated intensity in sub-nuclear foci in S phase (EdU-positive) cells of the experiment described in Figure 1D. Similar cell numbers were compared for the different conditions.

(F) Cell cycle distribution of PLA foci between wild-type RNF168 (WT and UBD) and PCNA.

(G and H) Cell cycle distribution of H2AK15Ub foci in EdU-positive cells.

All scale bars represent 10 μm. See also Figure S1.

Interestingly, these effects on DNA replication were not accompanied by detectable global DDR activation, as revealed by overall nuclear levels of H2A.X phosphorylation (γH2A.X, Figure 2A, right panel) and other canonical markers of checkpoint activation (KAP1-, CHK1- and RPA-phosphorylation; Figure 2D). To further exclude that this reduction in DNA synthesis upon RNF168 depletion is due to increased DNA damage, we performed a DNA comet assay comparing RNF168-proficient with RNF168-deficient cells. The two cell populations did not differ significantly, while cells treated with the DNA damaging agent camptothecin (CPT) expectedly show a marked accumulation of chromosomal breaks (Figures 2E and S2D). These data strongly suggest that the delayed fork progression observed in RNF168-defective cells does not reflect detectable accumulation of endogenous DNA damage and global DDR signaling.

We also used fibroblasts derived from a RIDDLE syndrome patient (RIDDLE cells) (Stewart et al., 2007),which contain inactivating mutations of the *RNF168* gene in both alleles, and the same cells complemented with HA-RNF168 as a reference (Stewart et al., 2009). Importantly, both the reduced EdU incorporation

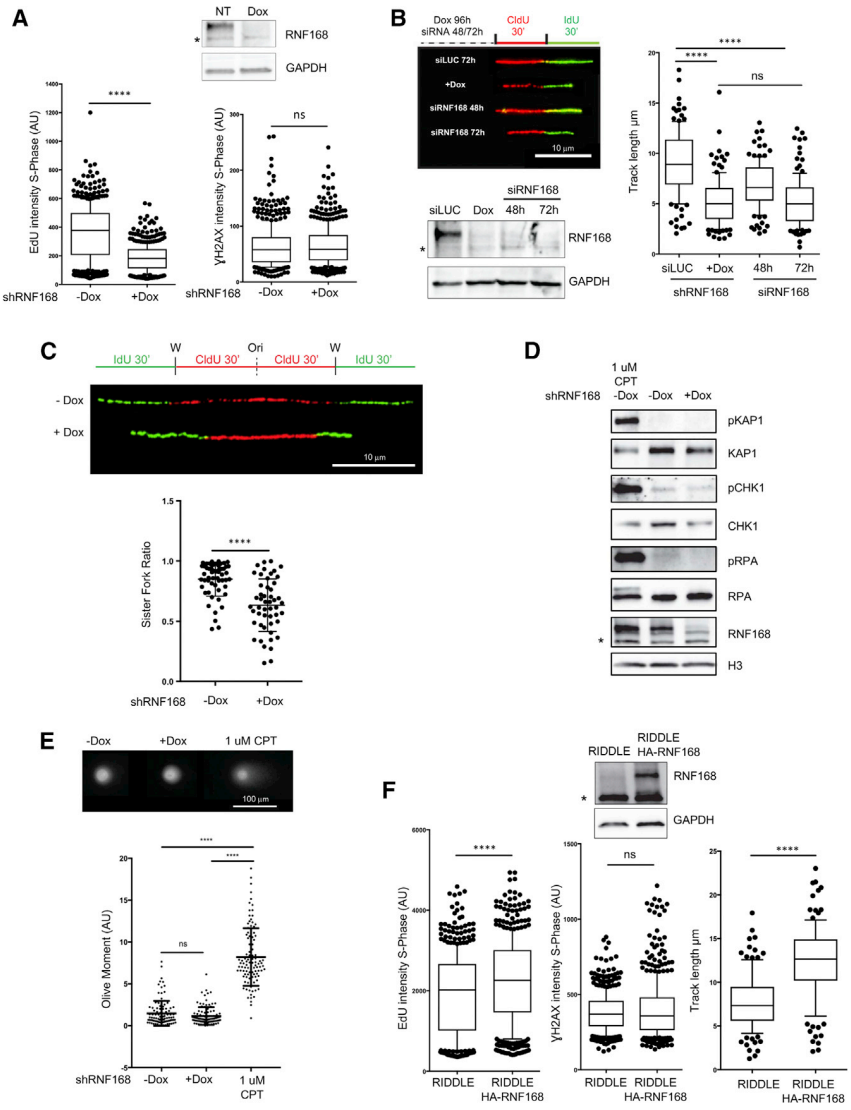

Figure 2. RNF168 Is Required for Efficient DNA Replication in Unperturbed Conditions

(A) EdU and γH2AX flow cytometry intensity values from S phase (EdU-positive) control (−Dox) and RNF168-depleted cells (+Dox). The intensity values of 500 EdU-positive cells per sample were extracted from the raw data and used for statistical analysis. The level of RNF168 depletion is shown.

(B) DNA fiber spreading analysis of control cells (siLUC, 72 hr) and cells depleted of RNF168 using either an inducible shRNA (+Dox) or an siRNA of a different sequence (siRNF168, 48 hr and 72 hr). A labeling scheme and fibers of representative size are shown for each condition in the top left panel. The level of RNF168 depletion is shown.

(C) Representative images of a symmetric and an asymmetric fork from U2OS shRNF168 cells. Quantification of the sister fork ratio in RNF168-proficient and -deficient cells is shown.

(D) Immunoblot analysis to follow checkpoint activation in control and RNF168-depleted cells using the indicated antibodies. Cells treated with 1 μM CPT serve as positive control for full DDR activation.

(E) Quantification of the olive moment in control and RNF168-depleted cells from a representative neutral comet assay experiment. 1 μM CPT treatment is used as a positive control for DNA double-strand break formation. Mean value and standard deviations are indicated as vertical lines for each sample.

(F) RIDDLE patient fibroblasts (RIDDLE) and the same cell line reconstituted with HA-RNF168 were analyzed as in (A) and (B). *RNF168* expression levels were analyzed by immunoblotting. Asterisks indicate unspecific signals.

****p value < 0.0001; whiskers, 10th–90th percentile. See also Figure S2.

rate and the slow-down in fork speed as displayed by DNA fiber track length are recapitulated in this experimental system and are suppressed by exogenous *RNF168* expression (Figures 2F and S2E).

Unperturbed RNF168-Deficient Cells Display Elevated Fork Reversal, Required for the Observed Fork Slowing

Recent evidence in human cells suggests that replication forks are frequently undergoing remodeling into four-way junctions (reversed forks) upon various types of exogenous replication stress or at endogenous difficult-to-replicate loci (Follonier et al., 2013; Neelsen and Lopes, 2015; Zellweger et al., 2015). Intriguingly, the regressed arm at these structures exposes a double-stranded DNA end, which strikingly resembles a DSB and may thus implicate the function of DSB-responding factors. To test the hypothesis that replication fork remodeling underlies the involvement of DDR factors in unperturbed replication, we employed an established electron microscopy (EM) protocol to stabilize and visualize *in vivo* the architecture of replication intermediates, in the presence or absence of RNF168. Strikingly, RNF168-deficient cells reproducibly showed a ~3-fold increased accumulation of reversed forks during unperturbed replication, compared to RNF168-proficient cells (Figures 3A and S3A–S3D; Table S1A), suggesting that RNF168 affects the dynamics of these remodeled replication intermediates. Reversed forks are transient intermediates, and their accumulation upon genotoxic treatments depends on the balance between promoting activities—such as the central recombinase RAD51 or the dsDNA translocases SMARCAL1 and ZRANB3—and restart/resolution factors, such as the RECQ1 helicase, which is negatively regulated by PARP1-dependent PARylation (Berti et al., 2013; Neelsen and Lopes, 2015 and references therein). Importantly, we found that preventing fork reversal by depleting either RAD51 or SMARCAL1 in RNF168-deficient cells completely restored normal rates of fork progression during unperturbed S phase (Figures 3B, 3C, S3E, and S3F), while depletion of ZRANB3—reportedly dispensable for endogenous levels of fork reversal (Vujanovic et al., 2017)—did not recapitulate the same effect (Figures 3D and S3G). Analogously, PARP inhibition restored

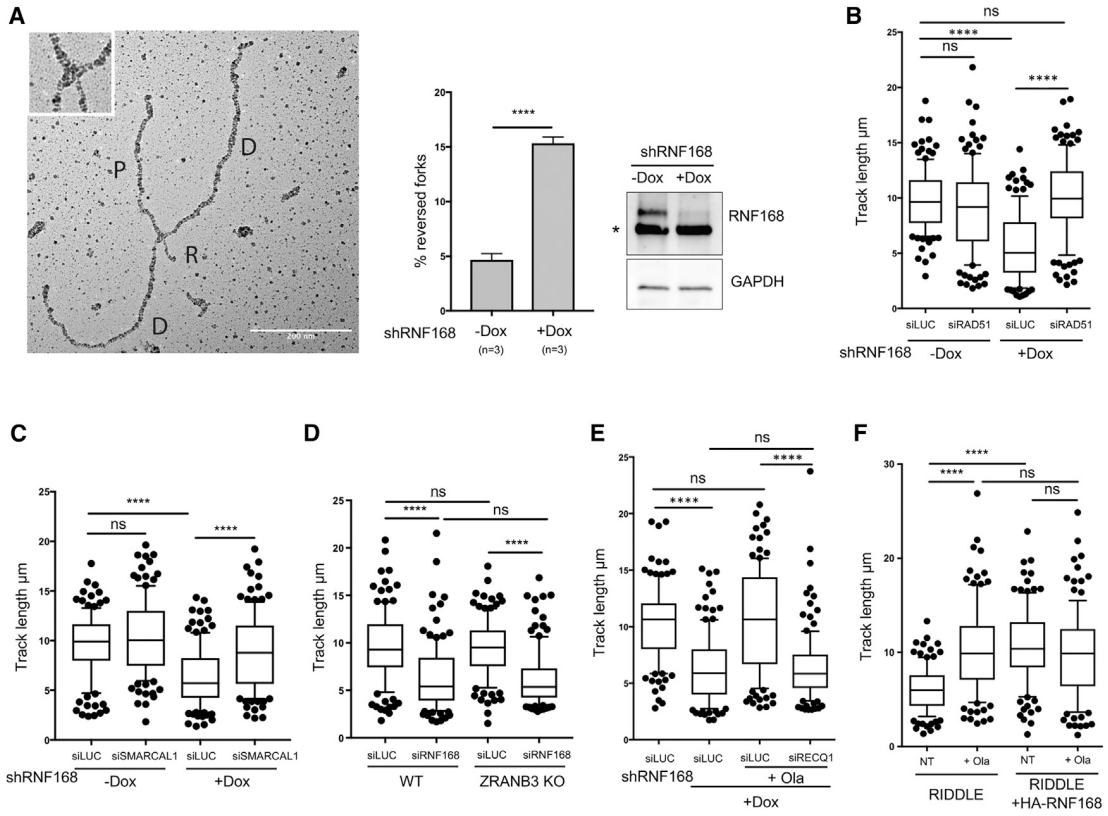

Figure 3. RNF168 Depletion Leads to Accumulation of Reversed Forks, Required for Fork Slowing

(A) Frequency of reversed replication forks in control and RNF168-depleted cells as found in three separate experiments by transmission electron microscopy (EM). At least 70 molecules were analyzed for each sample (***p value = 0.001, paired t test). An electron micrograph of a representative reversed replication fork is presented (P, parental duplex; D, daughter duplexes; R, regressed arm). *RNF168* expression was analyzed by immunoblotting (*unspecific band).

(B–D) DNA fiber spreading analysis in control cells (siLUC, −Dox) or in cells depleted of the indicated factors.

(E and F) DNA fiber spreading analysis investigating the effect of Olaparib treatment (Ola, 10 μM, 2 hr) on replication fork speed in RNF168-depleted cells (siLUC, +Ola, +Dox) and cells co-depleted of RNF168 and RECQ1 (siRECQ1, +Ola, +Dox) and in RIDDLE and RIDDLE HA-RNF168 fibroblasts.

****p value < 0.0001; whiskers, 10th–90th percentile. See also Figure S3.

efficient fork progression in RNF168-defective cells in a RECQ1-dependent manner (Figures 3E and S3H). Remarkably, PARP inhibition in RIDDLE cells also fully rescued efficient fork progression to the levels observed upon RNF168 complementation (Figures 3F and S3I). Altogether, these results indicate that replication fork reversal is a prerequisite for the defective fork progression observed upon RNF168 inactivation and suggest a potential role for RNF168 in promoting reversed fork restart. Furthermore, as RAD51 is strictly required for DSB repair, the suppression of fork slowing upon RAD51 inactivation strongly argues against accumulation of endogenous DSBs as the underlying mechanism of reduced fork progression in RNF168-defective cells. Along with the data in Figures 2D and 2E, this evidence further supports a DSB-independent role for RNF168 during unperturbed S phase.

Upstream and Downstream DDR Factors Are Epistatic to RNF168 for Its Replication Function

If the function of RNF168 in replication fork progression and remodeling truly reflects the formation of a double-stranded end at regressed arms, we reckoned that depletion of other DDR factors should result in similar defects. To address this point, we used various systems to target different DDR factors, alone or in combination with RNF168 depletion. First, we used shRNA-inducible U2OS cells to test the contribution of RNF8—which acts upstream of RNF168 in the DDR pathway—to unperturbed DNA replication. We found that, like RNF168, RNF8 depletion leads to a reduced rate of DNA synthesis—measured by EdU incorporation (Figure S4A)—and of replication fork progression (Figure 4A). Importantly, co-depletion of RNF8 and RNF168 did not lead to any further reduction in fork speed, suggesting that, in analogy to the DSB response, the two factors are epistatic. We obtained remarkably similar results in *53BP1* knockout U2OS cells, which displayed a reduced rate of DNA synthesis (Figure S4B) and fork progression that was not further exacerbated by concomitant RNF168 depletion (Figure 4B). Finally, we analyzed the contribution of ATM, the apical kinase of the DSB signaling pathway, responsible for RNF8/RNF168 recruitment at DSBs. We tested fork progression in U2OS shRNF168 cells optionally treated with the ATM inhibitor KU55933 and/or

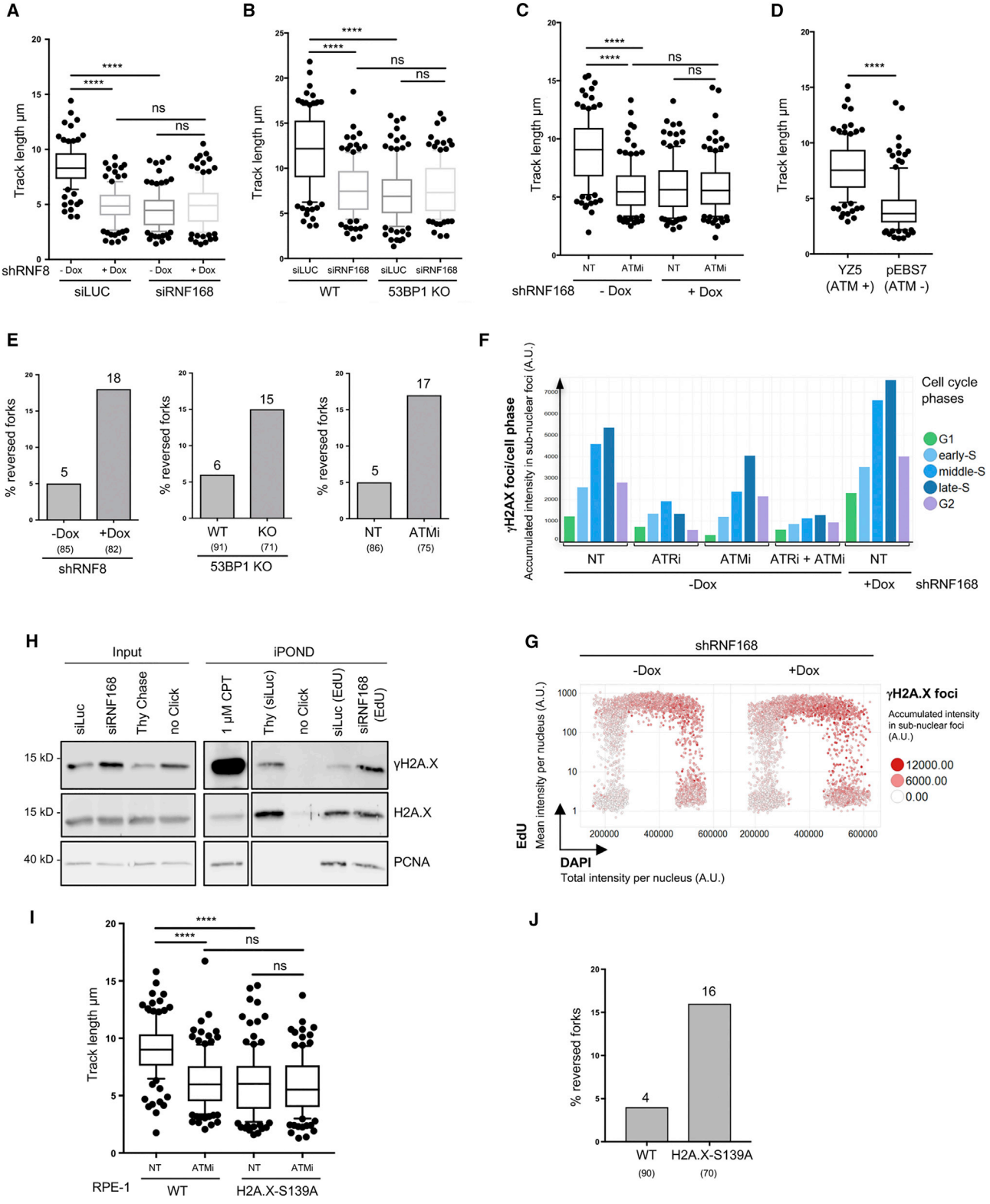

(legend on next page)

doxycycline to conditionally downregulate *RNF168*. In parallel, we analyzed fork progression in ataxia telangiectasia patient cells (AT22iJE-T), which carry inactivating mutations in the *ATM* gene, and in their complemented counterpart (Ziv et al., 1997). In both systems, we observed that ATM activity is required for efficient DNA replication: both pharmacological inhibition and genetic inactivation lead to reduced DNA fork progression during unperturbed S phase, which is again epistatic to the effects observed upon RNF168 inactivation (Figures 4C and 4D). Moreover, similarly to the effects reported in RNF168-deficient cells (Figure 3A), our EM analysis revealed a 2.5- to 3.5-fold accumulation of reversed forks in RNF8- and 53BP1-deficient U2OS cells, as well as upon ATM inhibition (Figure 4E; Table S1B–S1D). Importantly, BRCA1 depletion had only a marginal effect on replication fork progression, which was not epistatic to RNF168 depletion (Figure S4C), suggesting that RNF168's role in replication is independent of the downstream HR pathway.

Although these data clearly indicate that the ATM/RNF8/RNF168/53BP1 signaling pathway is required for efficient DNA replication in unperturbed S phase, we were puzzled by the absence of detectable checkpoint activation under these conditions (Figures 2A and 2D). We thus carefully monitored H2A.X phosphorylation throughout the cell cycle by QIBC analysis in U2OS shRNF168 cells. We found that cells in middle and late S phase do show detectable γH2A.X foci even in the absence of exogenous treatments (Figures 4F and S4D). This γH2A.X signal is specific and not cell line dependent, as it was readily detected also in RPE-1 cells but was abolished by H2A.X replacement with a non-phosphorylatable version (H2A.X-S139A; Figure S4E). Furthermore, this endogenous γH2A.X signal is largely reduced upon treatment with both ATR and ATM inhibitors (Figure 4F). Thus, despite undetectable global DDR activation (Figures 2A–2D), local ATR/ATM-mediated H2A.X phosphorylation detectably increases during cell cycle progression, reaching a peak in late S phase and correlating with other marks of activation of the DDR cascade (Figures 1E and 1H). Accordingly, blocking this signaling cascade downstream by RNF168 depletion did not affect global H2A.X phosphorylation, but induced local accumulation of γH2A.X in these endogenous foci (Figures 2A, 4F, 4G, and S4F). Similar conclusions could be drawn by iPOND (Sirbu et al., 2013), by which we found detectable levels of H2A.X phosphorylation directly at replication forks, which were increased upon RNF168 depletion (Figure 4H). Finally, we tested whether the impairment of endogenous H2A.X phosphorylation resulted in replication phenotypes similar to those observed upon other DDR defects. Using untransformed RPE-1 cells expressing either wild-type H2A.X or its phosphorylation mutant (S139A; Figure S4E), we found that—similarly to all other tested DDR defects (Figures 4A–4E)—defective H2A.X phosphorylation leads to accumulation of reversed forks and impaired replication fork progression and that the latter defect is epistatic to ATM inhibition (Figures 4I and 4J; Table S1E). Together, these results suggest that, despite undetectable global activation of the DDR, local H2A.X phosphorylation during unperturbed S phase engages classical DDR factors in controlling fork remodeling and promoting efficient fork progression.

Reduced Fork Speed upon RNF168 Depletion Depends on Nucleolytic Processing

Although fork reversal was proposed to assist fork integrity and restart upon replication stress (Neelsen and Lopes, 2015), it was also recently shown to trigger MRE11-dependent degradation of stalled forks under certain genetic perturbations, which mediates the chemosensitivity of BRCA-defective cells (Lemaçon et al., 2017; Mijic et al., 2017; Ray Chaudhuri et al., 2016). We thus tested whether MRE11-dependent degradation is also implicated in the defects in fork progression and architecture observed upon interference with the DDR pathway. Using mirin as a well-characterized inhibitor of MRE11 nuclease activity at replication forks (Schlacher et al., 2011), we found that MRE11 inhibition significantly restored replication fork progression in all tested systems of RNF168-, RNF8-, 53BP1-, ATM-, and γH2A.X-depletion/inactivation conditions (Figures 5A–5F). These data suggest that the fork slowing observed in all these conditions reflects increased MRE11 activity or accessibility to de-protected forks, leading to nucleolytic processing of newly synthesized DNA. In light of the limited processivity reported for cellular nucleases, the reduced track length observed upon DDR inactivation is unlikely to purely reflect degradation of nascent DNA. In fact, it may also result from impaired DNA synthesis while forks are engaged in unscheduled processing, ultimately leading to temporary fork stalling. Moreover, the partial rescue of fork speed observed upon mirin treatment might reflect the redundant action of nucleases other than MRE11 (Lemaçon et al., 2017) at replication forks destabilized by inactivation of the

Figure 4. Upstream and Downstream DDR Factors Share the Replication Function of RNF168 and Are Epistatic to It

(A and B) Statistical analysis of IdU track length measurements from a DNA fiber spreading experiment performed in cells with different genetic contexts, as indicated.

(C and D) DNA fiber spreading analysis of RNF168-proficient or -deficient cells (C) after pre-treating with an ATM inhibitor (ATMi) for 1 hr before labeling, of the ataxia telangiectasia patient fibroblast cell line AT22IJE-T carrying an empty expression vector (pEBS7), and of the same cell line expressing recombinant *ATM* (YZ5).

(E) Frequency of reversed replication forks observed by EM analysis in control cells and cells subjected to the depletion or inhibition of the indicated DDR factors.

(F) Quantification of γH2A.X accumulated intensity in sub-nuclear foci in different cell cycle phases in pre-extracted cells (see STAR Methods), treated as indicated.

(G) Representative cell cycle distribution of γH2A.X accumulated intensity in sub-nuclear foci of control and RNF168-depleted cells.

(H) Immunoblot showing γH2A.X protein levels in iPOND experiment in control and RNF168-depleted cells.

(I) DNA fiber spreading analysis in WT and H2A.X-S139A cells under untreated conditions (NT) or upon ATMi.

(J) Frequency of reversed replication forks in WT and H2A.X-S139A cells as observed by EM analysis. The numbers in brackets in E and L indicate the total of analyzed molecules, and the values written above the columns indicate the relative reversal frequencies. Results of an additional independent experiment are reported in Table S1. ****p value < 0.0001; whiskers, 10th–90th percentile. See also Figure S4.

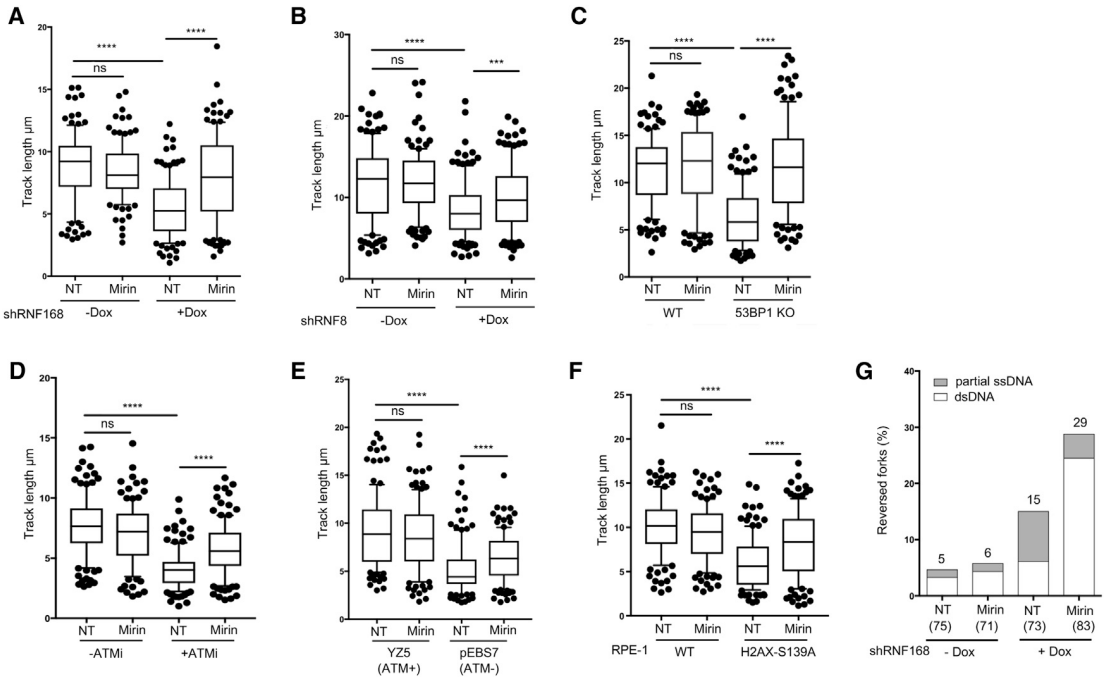

Figure 5. Reduced Fork Speed upon RNF168/RNF8/53BP1/ATM Depletion Depends on MRE11-Dependent Nucleolytic Processing

(A–F) DNA fiber spreading analysis of the effect of mirin treatment on the replication fork speed in different backgrounds, as indicated, or in combination with ATMi (D).

(G) Frequency of reversed replication forks observed by EM analysis in RNF168-proficient versus -deficient cells left untreated or treated with mirin. The regressed arms of reversed forks were inspected for single-stranded DNA stretches (ssDNA). The percentage of partially single-stranded regressed arms is indicated in gray and the percentage of completely single-stranded regressed arms in black. ****p value < 0.0001, ***p value 0.0002; whiskers, 10th–90th percentile. See also Figure S5 and Tables S1B and S1C.

DDR pathway. As reported (Mijic et al., 2017), mirin treatment per se did not affect the frequency of reversed forks. Surprisingly—and differently from what was reported at hydroxyurea-stalled forks upon BRCA defects (Lemaçon et al., 2017; Mijic et al., 2017)—mirin treatment in unperturbed RNF8-, RNF168-, or 53BP1-defective cells invariably led to further marked accumulation of reversed forks (Figures 5G, S5A, and S5B; Tables S1A–S1C). In both the presence and the absence of mirin, reversed forks accumulating upon RNF8, RNF168, or 53BP1 inactivation frequently exposed extended ssDNA stretches, further suggesting that inactivation of the DDR pathway promotes deregulated regressed arm resection in unperturbed conditions (Figures 5G, S5A, and S5B).

It is seemingly counterintuitive that inhibiting MRE11 activity rescues fork speed but leads to further accumulation of reversed forks upon inactivation of various DDR factors. However, it is important to note that DNA fiber spreading measures the rate of fork progression over a distance, while EM analysis provides snapshots of the most persisting intermediates along the path of active forks (Vindigni and Lopes, 2017). As discussed above, MRE11-dependent degradation of transiently reversed forks may counteract DNA synthesis under conditions of defective DDR, leading to slow fork progression as a net effect. Impairing this degradation would prevent fork backtracking and promote continued fork progression via resection-independent restart of reversed forks. However, the overload and/or the intrinsic slowness of this restart mechanism upon MRE11 inhibition may force forks to spend a higher fraction of time in the reversed state, explaining our EM observations. The marked accumulation of reversed forks observed by inactivation of MRE11 and the DDR pathway is particularly striking, considering that these cells are not exposed to exogenous sources of genotoxic stress. This suggests that the RNF168 pathway is essential to counteract regressed arm resection and to provide efficient restart of endogenously reversed forks, preventing their accumulation during unperturbed S phase.

RNF168-Dependent Histone H2A Ubiquitination Is Required for Efficient DNA Replication

A key event of the DSB signaling pathway is the ubiquitination of histone H2A on the N-terminal site K13/K15 promoted by RNF168 (Gatti et al., 2012; Mattiroli et al., 2012), which is required for the activation of the downstream signaling cascade, being directly recognized by 53BP1 (Fradet-Turcotte et al., 2013). Hence, we asked whether this histone mark is also essential for RNF168 function in DNA replication. To address this point, we took advantage of a single point mutation in RNF168 (R57D), which maintains the ubiquitinating capability but specifically impairs the ubiquitination of histone H2A (Mattiroli et al., 2012). We generated Flp-In T-REx U2OS stable cell lines expressing FLAG-RNF168 wild-type, UBD, and R57D—all designed to be resistant to siRNAs targeting endogenous *RNF168*—confirmed that they

had normal cell cycle progression, and used them to perform complementation experiments (Figures S6A–S6C). We were able to restore efficient fork progression in siRNF168-depleted cells by expressing wild-type *RNF168* but not with UBD nor with R57D mutants, clearly indicating that not only the proper localization of RNF168 but also its specific activity toward histone H2A are required to mediate efficient fork progression during unperturbed S phase (Figure 6A).

Regular Nucleosome Deposition Occurs on Regressed Arms

Next, we reasoned that if the RNF168-mediated ubiquitination of H2A is required for efficient DNA replication via controlled restart of reversed forks, we would expect its targets (i.e., nucleosomes) to be present on the fourth, regressed arms of these intermediates. To address this important point, we performed *in vivo* psoralen crosslinking, coupled to EM analysis in denaturing conditions. As psoralen only intercalates in linker DNA between nucleosomes, this analysis reveals the nucleosomal organization of replicating molecules as a string of single-stranded bubbles separated by psoralen crosslinks, while non-chromatinized DNA (e.g., mitochondrial DNA, Figure S6D) appears as uniformly crosslinked DNA (Lucchini and Sogo, 1995). To verify that reversed forks could be confidently identified by denaturing EM analysis, we analyzed two different conditions of reversed fork accumulation—i.e., RNF168 depletion and topoisomerase I poisoning by CPT (Ray Chaudhuri et al., 2012)—and confirmed that their frequency was very similar in standard (native) and denaturing EM analysis (Figure S6E). We then carefully inspected the appearance of the identified regressed arms and noticed that single-stranded bubbles could be readily detected on all reversed replication forks found (Figure 6B) and had standard size (~150 bp per nucleosome) and periodicity as detected on parental and replicated DNA (Figures 6C, S6F, and S6G). These data strongly suggest that, despite their transient nature, regressed arms are readily chromatinized and display standard nucleosomal organization, thereby offering targets for DDR-mediated modifications.

RNF168-Deficient Cells Show Defects in Replicating Repetitive Sequences and Accumulate Chromosomal Abnormalities in Mitosis

Taken together, the replication defects described above upon inactivation of RNF168 and other DDR factors could be explained by a role of these proteins in replicating genomic regions that are intrinsically difficult to replicate and are thus particularly prone to fork reversal. Repetitive sequences, notably abundant in the human genome, are known to induce replication fork slowing (Neil et al., 2017). Recently, expanded GAA/TTC sequences were shown to undergo frequent fork reversal under unperturbed conditions by bidimensional electrophoresis (2D gels) and EM analysis of chromatinized, SV40-based plasmids (Follonier et al., 2013). Transfecting this plasmid system in U2OS shRNF168 cells, we verified that control plasmids were replicated with similar efficiency in the presence or absence of RNF168 (Figure S7A). However, when the transfected plasmids contained expanded GAA/TTC regions, additional signals were readily detected by 2D gels, such as a spot on the Y arc due to fork pausing at repeats, a "X-spot" corresponding to triplex-mediated post-replicative junctions, and a spike signal—departing from the pausing spot and reaching just above the X-spot—which was shown to be highly enriched in forks reversed at the repetitive sequence (Figure 7A) (Follonier et al., 2013). Strikingly, by accurate quantification of 2D gels (Figure S7B) in two independent experiments, we reproducibly observed that the signal corresponding to reversed forks was specifically increased upon conditional RNF168 depletion (Figures 7A and S7C). Along with the data in Figure 3A, these results strongly suggest that RNF168 is required to prevent reversed fork accumulation at endogenous difficult-to-replicate regions, presumably by promoting effective reversed fork restart. In line with these replication problems, we observed that prolonged (1 week) RNF168 depletion in U2OS shRNF168 cells, as well as permanent RNF168 inactivation in RIDDLE cells, are associated with increased chromosome abnormalities in mitosis, mostly visible as regions of decondensed chromatin along metaphase chromatids (Figures 7B and S7D–S7F). The effect is exacerbated when DNA replication is challenged by treating cells with low-dose aphidicolin (Aph, Figure 7C). Similar observations have been reported upon other genetic perturbations increasing endogenous replication stress and bona fide reflect genomic regions where replication is not complete upon entry into mitosis (Bhowmick and Hickson, 2017).

DISCUSSION

We provide here several lines of evidence that well-established DDR factors of the RNF168 pathway play a crucial role to assist the replication process in the absence of any exogenous genotoxic stress. A link between this pathway and endogenous replication stress was proposed while describing 53BP1 nuclear bodies, as these G1 phase-specific nuclear accumulations of 53BP1 were linked to unresolved replication stress inherited from the previous S phase. However, these structures were suggested to arise via mitotic processing of these residual intermediates into DSBs, invoking the classical function of this pathway in DSB signaling and repair (Lukas et al., 2011). Similarly, Rad9/53BP1—along with its antagonistic partner, BRCA1—was also recently involved in mechanisms of stalled fork processing and restart upon genotoxic treatments (Her et al., 2018; Villa et al., 2018; Xu et al., 2017), but a potential role of DSB signaling factors at replication forks during unperturbed S phase has remained unexplored.

We now show that these factors are required for efficient replication fork progression even in the absence of exogenous stress and detectable DNA breakage or DSB signaling, identifying a new crucial role for this pathway in addition to its established role in the DSB response. Four important lines of evidence support a specific role for the RNF168-associated DDR pathway during unperturbed replication, independent of DSB formation: (1) RNF168 co-localizes and physically interacts with PCNA at a subset of replication factories in unperturbed conditions, which are not associated with detectable DDR activation or physical evidence of DNA breaks; (2) the replication function of RNF168 requires specific ubiquitination of histone H2A (H2AK15Ub), which is indeed cytologically detectable during unperturbed

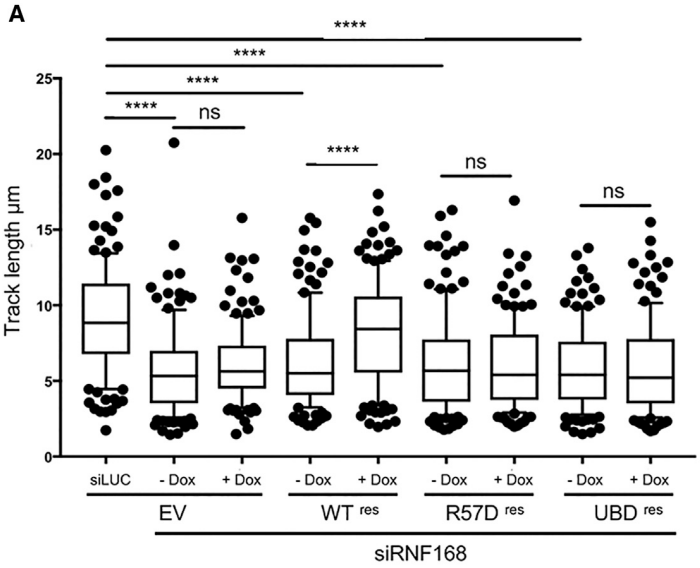

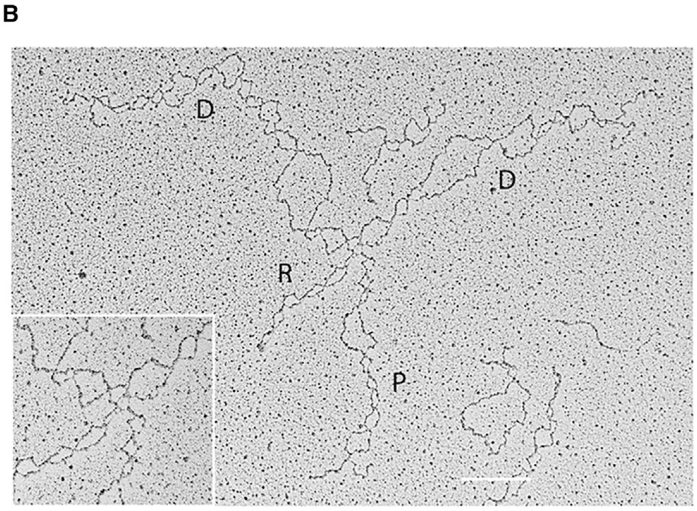

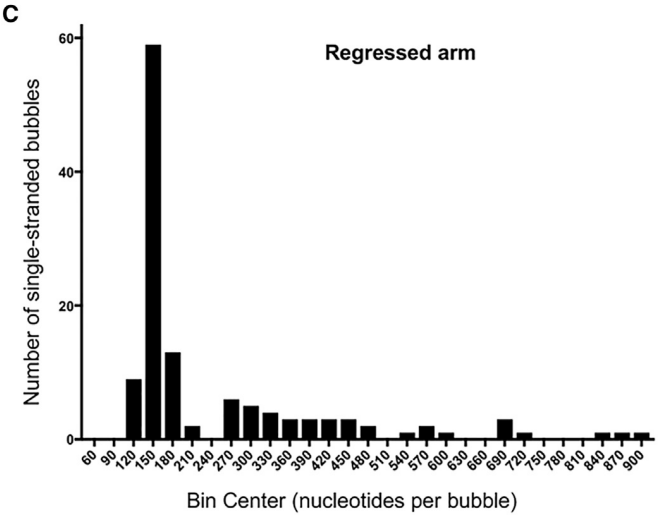

Figure 6. RNF168 Ubiquitin Ligase Activity on Histone H2A Is Required for Efficient DNA Replication

(A) DNA fiber spreading analysis of replication fork progression rate in U2OS Flp-In T-REx cell lines conditionally expressing siRNA-resistant forms of RNF168 WT and the indicated mutants. All four cell lines were depleted of endogenous RNF168 by siRNA transfection (siRNF168) 60 hr before Dox induction.

(B) Representative electron micrograph of a denatured reversed replication fork from U2OS cells depleted of RNF168 using an inducible shRNA (P, parental duplex; D, daughter duplexes; R, regressed arm). The white scale bar equals 200 nm.

(C) Frequency distribution of the single-stranded bubble size on the regressed arm as observed by EM of denatured reversed replication forks from cells treated with 50 nM CPT or from RNF168-depleted cells. Similar distributions were observed on the parental and the two daughter strands of the same molecules and are depicted in Figures S6E and S6F. ****p value < 0.0001; whiskers, 10th–90th percentile.

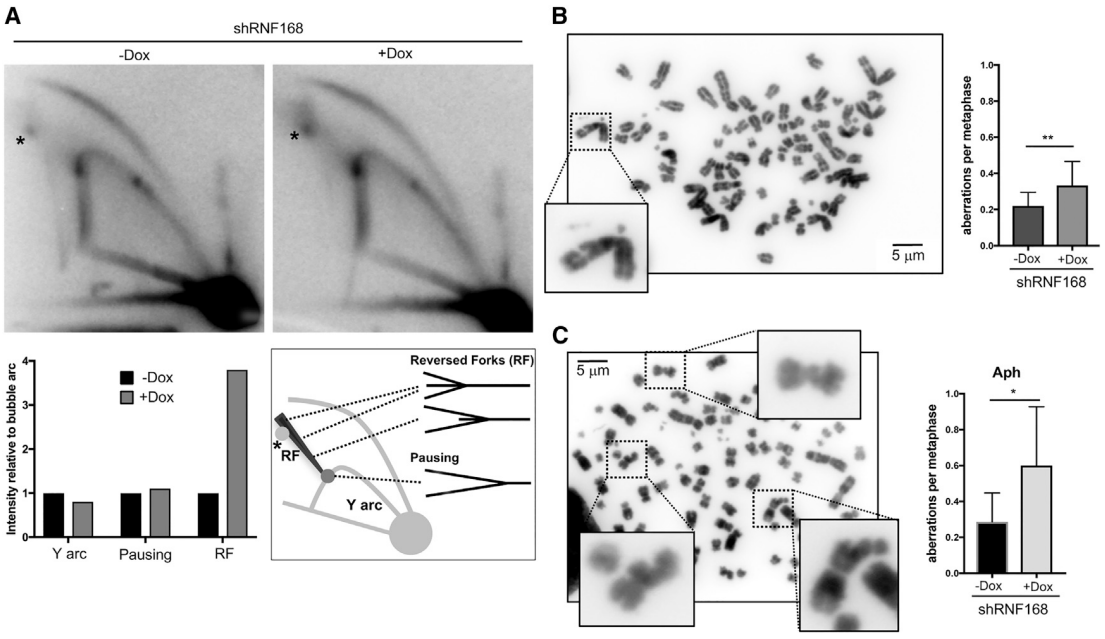

Figure 7. RNF168-Deficient Cells Show Defects in Replicating Repetitive Sequences, Resulting in Chromosomal Abnormalities

(A) Representative 2D gel analysis of an EcoRI-digested SV40-based plasmid containing 90 GAA/TTC repeats 48 hr after transfection into control and RNF168-depleted cells. Signals corresponding to different categories of replication intermediates were quantified as described in Figure S5A and depicted as bar plots for both samples. The graph on the right side explains the migration pattern of different replication intermediates of the used plasmid. The asterisk marks the so-called "X-spot," representing triplex-mediated junctions between replicated duplexes, reported to accumulate after replication of expanded GAA/TTC repeats (Follonier et al., 2013).

(B and C) Metaphase spreads to detect chromosomal aberrations in control and long-term RNF168-depleted cells (7 days) untreated (B) or treated with low dose of aphidicolin (C). Representative images are included. The graphs on the right depict the number of observed chromosomal abnormalities from three separate experiments.

See also Figure S7.

S phase; (3) even though global DDR activation is undetectable in unperturbed S phase, local ATR/ATM-dependent H2A.X phosphorylation can be monitored—especially in late S phase—and plays a key role upstream of RNF168 activation in mediating efficient replication fork progression; (4) RNF168 is required to limit the accumulation of unusual replication intermediates at a prototype of difficult-to-replicate regions—i.e., expanded GAA repeats—previously shown to induce transient fork slowing and remodeling.

These findings are reminiscent of the surprising evidence that key DNA repair factors—such as BRCA factors and Fanconi anemia proteins—play a genetically separable role in replication fork protection, which emerged as a key determinant of the chemosensitivity observed in BRCA-defective tumors (Ray Chaudhuri et al., 2016; Schlacher et al., 2012). Several groups reported that this clinically relevant, unscheduled nucleolytic degradation observed in BRCA-defective cancer cells is triggered by the remodeling of stalled forks into four-way junctions (Lemaçon et al., 2017; Mijic et al., 2017; Taglialatela et al., 2017). Analogously, Tel1—the yeast ATM ortholog—was recently reported to protect against degradation forks reversed upon topoisomerase I inhibition (Menin et al., 2018). Remarkably, using multiple genetic tools to interfere with replication fork remodeling (i.e., PARP inhibition and RAD51, SMARCAL1, or RECQ1 depletion), we found that the defects observed during unperturbed replication upon inactivation of RNF168 strictly depend on replication fork reversal. In light of the striking similarity between DSBs and double-stranded ends exposed at regressed arms, we propose that DSB signaling factors are recruited to remodeled replication forks and participate in modulating stability and restart of transiently stalled forks.

An important implication of our EM observations is that even during unperturbed S phase, a surprisingly high number of replication forks undergo reversal, imposing efficient fork restart mechanisms to prevent massive accumulation of reversed forks. Several chromosomal regions have been identified as "difficult-to-replicate," be it because of their repetitive nature, their propensity to form secondary structures, and/or their active transcription (Glover et al., 2017; Neil et al., 2017). Difficult-to-replicate regions tend to be replicated toward the end of S phase (Glover et al., 2017); interestingly, all marks of recruitment/activation of the RNF168 pathway—i.e., local γH2A.X, RNF168/PCNA proximity, and H2AK15Ub (Pellegrino et al., 2017)—are also enriched in late S phase. However, repetitive DNA represents up to 50% of all human genome, which may explain why most replication forks experience delayed progression upon inactivation of the DDR pathway during the standard labeling time of a fiber spreading experiment. It is likely that a large fraction of replication forks frequently undergo transient remodeling and require an active DDR pathway to efficiently drive fork

protection and restart. In that respect, RNF168 activation may consistently occur at replication forks, but the associated marks may become cytologically detectable only at chromosomal locations where fork pausing and reversal is less transient, i.e., at endogenous difficult-to-replicate regions, and/or where they inherently cluster, e.g., at condensed heterochromatic regions.

Another important implication of our data is that frequent, albeit transient, accumulation of double-stranded ends during fork remodeling implies an intrinsic risk of DDR activation, posing very similar issues to those extensively characterized at telomeres (Maciejowski and de Lange, 2017). However, even in genetic conditions that prevent a rapid turnover of reversed forks and thus lead to their accumulation and processing, we observed no detectable evidence of global DDR activation. It will be an interesting avenue of future research to clarify whether, similarly to telomeres, active mechanisms have evolved to finely control DDR activation from these endogenous DNA ends, which are associated with every unperturbed S phase and which certainly exceed telomeres in numbers. It is very likely that, despite the involvement of several classical DSB signaling factors in replication fork transactions, the DDR pathway may have specific mechanisms of signal amplification/limitation while playing its key role in unperturbed replication, in order to avoid interference with cell cycle progression. As shown here, detection of local and transient DDR activation during fork remodeling requires more refined experimental conditions than those extensively characterized in response to exogenous DNA damage.

How is the DDR pathway modulating the restart of reversed forks, limiting their accumulation? Our EM evidence suggests that inactivation of this pathway shifts the equilibrium of transiently stalled forks toward a reversed state and promotes nucleolytic processing of regressed arms, which at least partially limit accumulation of these structures in DDR-defective cells. As reversed fork restart was also shown to occur via both nucleolytic and non-nucleolytic pathways (Berti et al., 2013; Neelsen and Lopes, 2015), it is tempting to speculate that recruitment of these factors to the DNA end at regressed arms may limit access to nucleases. This may be achieved by direct protection of the end and/or by promoting an alternative pathway of reversed fork restart—e.g., via RECQ1-dependent branch migration—which does not implicate DNA end resection. Alternatively, and in analogy with its role in HR-mediated DSB repair (Smeenk and Mailand, 2016), RNF168-dependent chromatin ubiquitination may finely control regressed arm resection and promote RAD51-mediated fork protection and restoration mechanisms. Indeed, besides the well-established competition of 53BP1 and BRCA1 for DSB repair mechanism (Bunting et al., 2010), our data highlight the importance of ubiquitin-dependent 53BP1 functional recruitment in finely regulating the productive outcome of the recombination process, most likely by limiting unscheduled double-stranded end processing (Ochs et al., 2016). It will be important to explore specific protein partners of DDR factors during unperturbed S phase to gain mechanistic insight into the alternative function of these factors in replication.

The observation that regressed arms readily assemble nucleosomes is important and unexpected for structures that are inherently meant to be transient, as effective processing of these arms during fork restart would need nucleosome eviction. However, we reckon that nucleosome deposition on all DNA branches at the replication fork is passively accomplished, as it would be mechanistically difficult for the nucleosome deposition apparatus to distinguish regressed arms from standard replicated duplexes. Moreover, it would also be risky for the cells to have non-chromatinized DNA in proximity to paused replication forks, as this would increase the risk of unscheduled nucleolytic processing and chromosomal rearrangements. In fact, the evidence that nucleosomes are deposited on regressed arms—which were recently identified as entry points for fork degradation—suggests that histone modifications may be crucial determinants for the necessary equilibrium between DNA synthesis and degradation that assists efficient fork pausing and restart. This is in keeping with growing evidence that histone methylases such as MLL3/4 and SETD1A and chromatin remodelers such as CHD4 play critical roles in modulating fork accessibility by active nucleases, such as MRE11 (Higgs et al., 2018; Ray Chaudhuri et al., 2016). It will be a challenging but crucial task for future research to establish methods to specifically isolate and analyze the dynamic composition of nascent chromatin at regressed arms. Besides assessing the direct binding of DSB processing and signaling factors, such experiments promise to reveal the complex cellular apparatus, as well as epigenetic modifications, modulating reversed fork stability and restart. These studies may significantly help to shed light on mechanisms of genome instability during cellular proliferation and on patient-specific responses to chemotherapeutic treatments interfering with replication.

Overall, this work directly involves key DDR factors in the molecular mechanisms promoting efficient replication during unperturbed conditions. Some of the phenotypes associated with inactivation of these factors—such as immunodeficiency and radiosensitivity—are clearly linked to their role in the DSB response (Jackson and Bartek, 2009). However, it is tempting to speculate that other phenotypes associated with DDR inactivation at cellular levels—i.e., chromosomal instability—or in specific DDR-defective animal models and patients may also reflect the alternative role in unperturbed replication that we propose here for this signaling cascade.

STAR★METHODS

Detailed methods are provided in the online version of this paper and include the following:

- KEY RESOURCES TABLE
- CONTACT FOR REAGENT AND RESOURCE SHARING
- EXPERIMENTAL MODEL AND SUBJECT DETAILS
  - U2OS shRNF168
  - U2OS shRNF8
  - U2OS 53BP1 KO and matching WT U2OS
  - RIDDLE and RIDDLE HA-RNF168
  - U2OS
  - AT22IJE-T cell lines
  - U2OS Flp-In T-REx cell lines
  - RPE H2AX S139A and matching WT RPE
  - U2OS ZRANB3 KO

SUPPLEMENTAL INFORMATION

Supplemental Information includes seven figures and one table and can be found with this article online at https://doi.org/10.1016/j.molcel.2018.07.011.

ACKNOWLEDGMENTS

We thank G. Stewart, J. Lukas, S. Jackson, N. Mailand, D. Durocher, and Y. Shiloh for providing valuable cell lines; M. Altmeyer and F. Teloni for support with QIBC studies; the Center for Microscopy and Image Analysis of the University of Zurich for assistance with electron microscopy and imaging analysis; and A. Weber, M. Healy, K. Mutreja, R. Zellweger, M.S. Walser, M. Gatti, and all members of the Lopes and Penengo labs for technical assistance and discussions. We thank J. Lukas and M. Altmeyer for useful suggestions on the project. This work was supported by the SNF grant 31003A_169959, the ERC Consolidator Grant 617102, and the Swiss Cancer League grant KFS-3967-08-2016 to M.L. and by the SNF grant 31003A_166370, the Helmut Horten grant, and the Novartis grant (17A039) to L.P. M.B. was supported by the Marie Skłodowska-Curie postdoctoral fellowship (704817).

AUTHOR CONTRIBUTIONS

J.A.S. performed and analyzed all EM, flow cytometry, DNA fiber experiments, comet assays, and immunofluorescence studies of γH2A.X; M.B. and F.W. performed additional immunofluorescence, QIBC, and PLA; M.C.R. performed metaphase spreads; J.K. and F.S. assisted with biochemical studies; H.S. and K.Z. performed 2D gels; S.U. assisted with EM analysis; R.F. generated antibodies; M.L. and L.P. designed the experiments and wrote the manuscript, assisted by J.A.S.

DECLARATION OF INTERESTS

We declare no conflicts of interest.

Received: January 19, 2018
Revised: June 1, 2018
Accepted: July 11, 2018
Published: August 16, 2018

REFERENCES

Berti, M., Ray Chaudhuri, A., Thangavel, S., Gomathinayagam, S., Kenig, S., Vujanovic, M., Odreman, F., Glatter, T., Graziano, S., Mendoza-Maldonado, R., et al. (2013). Human RECQ1 promotes restart of replication forks reversed by DNA topoisomerase I inhibition. Nat. Struct. Mol. Biol. *20*, 347–354.

Bhowmick, R., and Hickson, I.D. (2017). The "enemies within": regions of the genome that are inherently difficult to replicate. F1000Res. *6*, 666.

Bunting, S.F., Callén, E., Wong, N., Chen, H.T., Polato, F., Gunn, A., Bothmer, A., Feldhahn, N., Fernandez-Capetillo, O., Cao, L., et al. (2010). 53BP1 inhibits homologous recombination in Brca1-deficient cells by blocking resection of DNA breaks. Cell *141*, 243–254.

Follonier, C., Oehler, J., Herrador, R., and Lopes, M. (2013). Friedreich's ataxia-associated GAA repeats induce replication-fork reversal and unusual molecular junctions. Nat. Struct. Mol. Biol. *20*, 486–494.

Fradet-Turcotte, A., Canny, M.D., Escribano-Díaz, C., Orthwein, A., Leung, C.C., Huang, H., Landry, M.C., Kitevski-LeBlanc, J., Noordermeer, S.M., Sicheri, F., and Durocher, D. (2013). 53BP1 is a reader of the DNA-damage-induced H2A Lys 15 ubiquitin mark. Nature *499*, 50–54.

Gatti, M., Pinato, S., Maspero, E., Soffientini, P., Polo, S., and Penengo, L. (2012). A novel ubiquitin mark at the N-terminal tail of histone H2As targeted by RNF168 ubiquitin ligase. Cell Cycle *11*, 2538–2544.

Gatti, M., Pinato, S., Maiolica, A., Rocchio, F., Prato, M.G., Aebersold, R., and Penengo, L. (2015). RNF168 promotes noncanonical K27 ubiquitination to signal DNA damage. Cell Rep. *10*, 226–238.

Glover, T.W., Wilson, T.E., and Arlt, M.F. (2017). Fragile sites in cancer: more than meets the eye. Nat. Rev. Cancer *17*, 489–501.

Hashimoto, Y., Ray Chaudhuri, A., Lopes, M., and Costanzo, V. (2010). Rad51 protects nascent DNA from Mre11-dependent degradation and promotes continuous DNA synthesis. Nat. Struct. Mol. Biol. *17*, 1305–1311.

Her, J., Ray, C., Altshuler, J., Zheng, H., and Bunting, S.F. (2018). 53BP1 Mediates ATR-Chk1 Signaling and Protects Replication Forks under Conditions of Replication Stress. Mol. Cell. Biol. *38*, e00472-17.

Higgs, M.R., Sato, K., Reynolds, J.J., Begum, S., Bayley, R., Goula, A., Vernet, A., Paquin, K.L., Skalnik, D.G., Kobayashi, W., et al. (2018). Histone Methylation by SETD1A Protects Nascent DNA through the Nucleosome Chaperone Activity of FANCD2. Mol. Cell *71*, 25–41.e6.

Jackson, S.P., and Bartek, J. (2009). The DNA-damage response in human biology and disease. Nature *461*, 1071–1078.

Jackson, D.A., and Pombo, A. (1998). Replicon clusters are stable units of chromosome structure: evidence that nuclear organization contributes to the efficient activation and propagation of S phase in human cells. J. Cell Biol. *140*, 1285–1295.

Lemaçon, D., Jackson, J., Quinet, A., Brickner, J.R., Li, S., Yazinski, S., You, Z., Ira, G., Zou, L., Mosammaparast, N., and Vindigni, A. (2017). MRE11 and EXO1 nucleases degrade reversed forks and elicit MUS81-dependent fork rescue in BRCA2-deficient cells. Nat. Commun. *8*, 860.

Lucchini, R., and Sogo, J.M. (1995). Replication of transcriptionally active chromatin. Nature *374*, 276–280.

Lukas, C., Savic, V., Bekker-Jensen, S., Doil, C., Neumann, B., Pedersen, R.S., Grøfte, M., Chan, K.L., Hickson, I.D., Bartek, J., and Lukas, J. (2011). 53BP1 nuclear bodies form around DNA lesions generated by mitotic transmission of chromosomes under replication stress. Nat. Cell Biol. *13*, 243–253.

Maciejowski, J., and de Lange, T. (2017). Telomeres in cancer: tumour suppression and genome instability. Nat. Rev. Mol. Cell Biol. *18*, 175–186.

Mattiroli, F., Vissers, J.H., van Dijk, W.J., Ikpa, P., Citterio, E., Vermeulen, W., Marteijn, J.A., and Sixma, T.K. (2012). RNF168 ubiquitinates K13-15 on H2A/H2AX to drive DNA damage signaling. Cell *150*, 1182–1195.

Menin, L., Ursich, S., Trovesi, C., Zellweger, R., Lopes, M., Longhese, M.P., and Clerici, M. (2018). Tel1/ATM prevents degradation of replication forks that reverse after topoisomerase poisoning. EMBO Rep. *19*, e45535.

Mijic, S., Zellweger, R., Chappidi, N., Berti, M., Jacobs, K., Mutreja, K., Ursich, S., Ray Chaudhuri, A., Nussenzweig, A., Janscak, P., and Lopes, M. (2017).

Replication fork reversal triggers fork degradation in BRCA2-defective cells. Nat. Commun. *8*, 859.

Neelsen, K.J., and Lopes, M. (2015). Replication fork reversal in eukaryotes: from dead end to dynamic response. Nat. Rev. Mol. Cell Biol. *16*, 207–220.

Neil, A.J., Kim, J.C., and Mirkin, S.M. (2017). Precarious maintenance of simple DNA repeats in eukaryotes. BioEssays *39*. Published online July 13, 2017. https://doi.org/10.1002/bies.201700077.

Ochs, F., Somyajit, K., Altmeyer, M., Rask, M.B., Lukas, J., and Lukas, C. (2016). 53BP1 fosters fidelity of homology-directed DNA repair. Nat. Struct. Mol. Biol. *23*, 714–721.

Pellegrino, S., Michelena, J., Teloni, F., Imhof, R., and Altmeyer, M. (2017). Replication-Coupled Dilution of H4K20me2 Guides 53BP1 to Pre-replicative Chromatin. Cell Rep. *19*, 1819–1831.

Penengo, L., Mapelli, M., Murachelli, A.G., Confalonieri, S., Magri, L., Musacchio, A., Di Fiore, P.P., Polo, S., and Schneider, T.R. (2006). Crystal structure of the ubiquitin binding domains of rabex-5 reveals two modes of interaction with ubiquitin. Cell *124*, 1183–1195.

Petermann, E., and Helleday, T. (2010). Pathways of mammalian replication fork restart. Nat. Rev. Mol. Cell Biol. *11*, 683–687.

Pinato, S., Gatti, M., Scandiuzzi, C., Confalonieri, S., and Penengo, L. (2011). UMI, a novel RNF168 ubiquitin binding domain involved in the DNA damage signaling pathway. Mol. Cell. Biol. *31*, 118–126.

Ray Chaudhuri, A., Hashimoto, Y., Herrador, R., Neelsen, K.J., Fachinetti, D., Bermejo, R., Cocito, A., Costanzo, V., and Lopes, M. (2012). Topoisomerase I poisoning results in PARP-mediated replication fork reversal. Nat. Struct. Mol. Biol. *19*, 417–423.

Ray Chaudhuri, A., Callen, E., Ding, X., Gogola, E., Duarte, A.A., Lee, J.E., Wong, N., Lafarga, V., Calvo, J.A., Panzarino, N.J., et al. (2016). Replication fork stability confers chemoresistance in BRCA-deficient cells. Nature *535*, 382–387.

Schlacher, K., Christ, N., Siaud, N., Egashira, A., Wu, H., and Jasin, M. (2011). Double-strand break repair-independent role for BRCA2 in blocking stalled replication fork degradation by MRE11. Cell *145*, 529–542.

Schlacher, K., Wu, H., and Jasin, M. (2012). A distinct replication fork protection pathway connects Fanconi anemia tumor suppressors to RAD51-BRCA1/2. Cancer Cell *22*, 106–116.

Sirbu, B.M., McDonald, W.H., Dungrawala, H., Badu-Nkansah, A., Kavanaugh, G.M., Chen, Y., Tabb, D.L., and Cortez, D. (2013). Identification of proteins at active, stalled, and collapsed replication forks using isolation of proteins on nascent DNA (iPOND) coupled with mass spectrometry. J. Biol. Chem. *288*, 31458–31467.

Smeenk, G., and Mailand, N. (2016). Writers, Readers, and Erasers of Histone Ubiquitylation in DNA Double-Strand Break Repair. Front. Genet. *7*, 122.

Specks, J., Nieto-Soler, M., Lopez-Contreras, A.J., and Fernandez-Capetillo, O. (2015). Modeling the study of DNA damage responses in mice. Methods Mol. Biol. *1267*, 413–437.

Stewart, G.S., Stankovic, T., Byrd, P.J., Wechsler, T., Miller, E.S., Huissoon, A., Drayson, M.T., West, S.C., Elledge, S.J., and Taylor, A.M. (2007). RIDDLE immunodeficiency syndrome is linked to defects in 53BP1-mediated DNA damage signaling. Proc. Natl. Acad. Sci. USA *104*, 16910–16915.

Stewart, G.S., Panier, S., Townsend, K., Al-Hakim, A.K., Kolas, N.K., Miller, E.S., Nakada, S., Ylanko, J., Olivarius, S., Mendez, M., et al. (2009). The RIDDLE syndrome protein mediates a ubiquitin-dependent signaling cascade at sites of DNA damage. Cell *136*, 420–434.

Taglialatela, A., Alvarez, S., Leuzzi, G., Sannino, V., Ranjha, L., Huang, J.W., Madubata, C., Anand, R., Levy, B., Rabadan, R., et al. (2017). Restoration of Replication Fork Stability in BRCA1- and BRCA2-Deficient Cells by Inactivation of SNF2-Family Fork Remodelers. Mol. Cell *68*, 414–430.e8, e418.

Toledo, L.I., Altmeyer, M., Rask, M.B., Lukas, C., Larsen, D.H., Povlsen, L.K., Bekker-Jensen, S., Mailand, N., Bartek, J., and Lukas, J. (2013). ATR prohibits replication catastrophe by preventing global exhaustion of RPA. Cell *155*, 1088–1103.

Villa, M., Bonetti, D., Carraro, M., and Longhese, M.P. (2018). Rad9/53BP1 protects stalled replication forks from degradation in Mec1/ATR-defective cells. EMBO Rep. *19*, 351–367.

Vindigni, A., and Lopes, M. (2017). Combining electron microscopy with single molecule DNA fiber approaches to study DNA replication dynamics. Biophys. Chem. *225*, 3–9.

Vujanovic, M., Krietsch, J., Raso, M.C., Terraneo, N., Zellweger, R., Schmid, J.A., Taglialatela, A., Huang, J.W., Holland, C.L., Zwicky, K., et al. (2017). Replication Fork Slowing and Reversal upon DNA Damage Require PCNA Polyubiquitination and ZRANB3 DNA Translocase Activity. Mol. Cell *67*, 882–890.e5.

Xu, Y., Ning, S., Wei, Z., Xu, R., Xu, X., Xing, M., Guo, R., and Xu, D. (2017). 53BP1 and BRCA1 control pathway choice for stalled replication restart. eLife *6*, e30523.

Zellweger, R., Dalcher, D., Mutreja, K., Berti, M., Schmid, J.A., Herrador, R., Vindigni, A., and Lopes, M. (2015). Rad51-mediated replication fork reversal is a global response to genotoxic treatments in human cells. J. Cell Biol. *208*, 563–579.

Zellweger, R., and Lopes, M. (2018). Dynamic Architecture of Eukaryotic DNA Replication Forks In Vivo, Visualized by Electron Microscopy. Methods Mol. Biol. *1672*, 261–294.

Ziv, Y., Bar-Shira, A., Pecker, I., Russell, P., Jorgensen, T.J., Tsarfati, I., and Shiloh, Y. (1997). Recombinant ATM protein complements the cellular A-T phenotype. Oncogene *15*, 159–167.

STAR★METHODS

KEY RESOURCES TABLE

REAGENT or RESOURCE	SOURCE	IDENTIFIER
Antibodies		
anti-γH2AX antibody (flow cytometry)	EMD Millipore	Cat# 05-636; RRID: AB_309864
anti-γH2AX antibody (QIBC)	Cell Signaling Technology	Cat# 9718; RRID: AB_2118009
anti-H2AX antibody	Abcam	Cat# ab11175; RRID: AB_297814
anti-RPA pS4/S8	Bethyl Laboratories	Cat# A300-245A; RRID: AB_210547
anti-KAP1 pS824	Behyl Laboratories	Cat# A300-767A; RRID: AB_669740
anti-KAP1	Bethyl Laboratories	Cat# A300-274A; RRID: AB_185559
anti-RPA32	Bethyl Laboratories	Cat# A300-244A; RRID: AB_185548
anti-mouse Alexa 546	Life Technologies	Cat# A11003; RRID: AB_141370
anti-rabbit Alexa 488	Life Technologies	Cat# A11008; RRID: AB_143165
anti-rabbit Alexa 555	Life Technologies	Cat# A21428; RRID: AB_141784
anti-mouse Alexa 647	Life Technologies	Cat# A21235; RRID: AB_141693
anti-mouse Alexa 488 (Fibers)	Life Technologies	Cat# A10011; RRID: AB_2534069
anti-mouse Alexa 488 (Immunofluorescence)	Immunological Sciences	Cat# IS-20010
anti-rat Cy3	Jackson ImmunoResearch	Cat# 712-165-513; RRID: AB_2340669
anti-CHK1pS345	Cell Signaling Technology	Cat# 2348; RRID: AB_331212
anti-FLAG rabbit	Sigma-Aldrich	Cat# F7425; RRID: AB_439687
anti-FLAG mouse M2 clone	Sigma-Aldrich	Cat# F1804; RRID: AB_262044
anti-CHK1	Santa Cruz	Cat# sc-8408; RRID: AB_627257
anti-Rad51	Santa Cruz	Cat# sc-8349; RRID: AB_2253533
anti-PCNA PC10	Santa Cruz	Cat# sc-56; RRID: AB_628110
anti-RNF168	R. Freire lab Instituto de Tecnologías Biomédicas, Tenerife, Spain	N/A
anti-RNF8	R. Freire lab Instituto de Tecnologías Biomédicas, Tenerife, Spain	N/A
anti-GAPDH	Millipore	Cat# MAB374; RRID: AB_2107445
anti-mouse HRP conjugate	GE Healthcare	Cat# NA931V
anti-rabbit HRP conjugate	GE Healthcare	Cat# NA934V
Rat anti-BrdU/CldU	Abcam	Cat# ab6326; RRID: AB_305426
anti-53BP1	Abcam	Cat# ab36823; RRID: AB_722497
anti-BrdU/IdU	BD Biosciences	Cat# 347580; RRID: AB_10015219
anti-RECQ1	Sigma-Aldrich	Cat# ABC1428
anti-B tubulin	Santa Cruz	Cat# sc-9104; RRID: AB_2241191
anti-H2A K15ub	Z. Zhang lab Mayo Clinic College of Medicine, Rochester, Minnesota, USA	N/A
Chemicals, Peptides, and Recombinant Proteins		
4,5′,8-trimethylpsoralen	Sigma-Aldrich	Cat# 512-56-1
2-Mercaptoethanol	Sigma-Aldrich	Cat# M3148
jetPRIME	Polyplus transfection	Cat# 114-01
Doxycycline hyclate	Sigma-Aldrich	Cat# D9891
5-Chloro-2′-deoxyuridine	Sigma-Aldrich	Cat#C6891
5-Iodo-2′-deoxyuridine	Sigma-Aldrich	Cat#I7125
Proteinase K, recombinant, PCR Grade	Sigma-Aldrich	Cat# 03115852001
Blasticidin	InvivoGen	Cat# ant-bl-05
Puromycin	InvivoGen	Cat# ant-pr-05

(*Continued on next page*)

Continued

REAGENT or RESOURCE	SOURCE	IDENTIFIER
Hygromycin B Gold	InvivoGen	Cat# ant-hg-05
Olaparib	Selleckchem	Cat# S1060
KU-55933 (ATMi)	Sigma-Aldrich	Cat# SML1109
Mirin	Sigma-Aldrich	Cat# M9948
PvuII high fidelity	New England Biolabs	Cat# R3151S
pOG44 Flp-Recombinase Expression Vector	Thermo Fisher	Cat# V600520
VECTASHIELD Antifade Mounting Medium	Vector Laboratories	Cat# H-1200
Prolong Gold antifade Mountant	Thermo Fisher	Cat# P36930
Nocodazole	Sigma-Aldrich	Cat# M1404
EcoRI	BioLabs	Cat# R0101S
DpnI	BioLabs	Cat# R0176L
RO-3306	Sigma-Aldrich	Cat# SML0569-5MG
Aphidicolin	Sigma-Aldrich	Cat# A0781-5MG
Colcemid	Thermo Fisher	Cat# 15210040
XmnI	BioLabs	Cat# R0194L
Zeta-probe membranes	Bio-Rad	Cat# 1620153
Critical Commercial Assays		
Click-iT EdU Alexa Fluor 488 Flow Cytometry Assay Kit (flow cytometry)	Thermo Fisher Scientific	Cat# C10425
Click-iT EdU Alexa Fluor 647 Imaging Kit (Immunofluorescence)	Thermo Fisher Scientific	Cat# C10340
Comet Assay 2 Well ES Unit with Starter Kit	Trevigen	Cat# 4250-050-ESK
QIAGEN-tip 20 Plasmid Mini Kit	QIAGEN	Cat# 10023
Amicon ultra 100K membrane size-exclusion columns	Millipore	Cat# UFC510096
Duolink *In Situ* Orange Starter Kit Mouse/Rabbit	Sigma-Aldrich	Cat# DUO92102
Mitochondrial DNA Isolation Kit	Abnova	Cat# KA0895
QIAprep Spin Miniprep kit	QIAGEN	Cat# 27104
Deposited Data		
Raw imaging data	This paper	https://doi.org/10.17632/hkjz8w9c6p.1
Experimental Models: Cell Lines		
U2OS	ATCC	HTB-96
53BP1 WT U2OS	Steve Jackson lab Wellcome Trust/ Cancer Research UK	N/A
53BP1 KO U2OS	Steve Jackson lab Wellcome Trust/ Cancer Research UK	N/A
U2OS shRNF168	Jiri Lukas lab University of Copenhagen Denmark	N/A
U2OS shRNF8	Niels Mailand lab University of Copenhagen Denmark	N/A
RIDDLE patient fibroblasts	Grant Stewart lab University of Birmingham UK	N/A
RIDDLE patient fibroblasts HA-RNF168	Grant Stewart lab University of Birmingham UK	N/A
RPE H2AX S139A	Steve Jackson lab Wellcome Trust/ Cancer Research UK	N/A
RPE WT (Matched with H2AX S139A)	Steve Jackson lab Wellcome Trust/ Cancer Research UK	N/A
U2OS ZRANB3 wild type control	David Cortez lab Vanderbilt University USA	N/A

(*Continued on next page*)

Continued

REAGENT or RESOURCE	SOURCE	IDENTIFIER
U2OS ZRANB3 knock out (clone 38)	David Cortez lab Vanderbilt University USA	N/A
AT22IJE-T (pEBS7)	Yossi Shiloh lab Tel Aviv University Israel	N/A
AT22IJE-T (YZ5)	Yossi Shiloh lab Tel Aviv University Israel	N/A
Oligonucleotides		
siRAD51: GACUGCCAGGAUAAAGCUUdTdT	Microsynth	N/A
siLuc: CGUACGCGGAAUACUUCGAUUdTdT	Microsynth	N/A
siRNF168: CGUGGAACUGUGGACGAUAA UUCAAdTdT	Microsynth	N/A
siSmarcal1: AAGCAAGGCCCAUCCCAAAdTdT	Microsynth	N/A
siBRCA1: GGAACCUGUCUCCACAAAGdTdT	Microsynth	N/A
SMART pool against human RECQ1	Dharmacon	NM_032941
Software and Algorithms		
GraphPad Prism7 for MAC OS X	GraphPad Software	https://www.graphpad.com/
ImageJ64 (DNA fiber length analysis and EM data)	ImageJ Software	https://imagej.nih.gov/ij/
Fiji (Comets)	ImageJ Software	https://imagej.nih.gov/ij/
FlowJo (Facs data analysis)	FlowJo Software	https://www.flowjo.com/
Attune Nxt (flow cytometry data acquisition)	Attune NxT Software	https://www.thermofisher.com/
Olympus ScanR Image Analysis Software Version 2.5.1 (QIBC data analysis)	Olympus Corporation	https://www.olympus-ims.com/en/microscope/software/
Spotfire data visualization software version 5.0.0 (QIBC data analysis)	TIBCO Software Inc.	https://spotfire.tibco.com/
FusionCapt Advance Solo 7 17.02 control and analysis software for chemiluminescence detection (used for western blot)	Vilber Lourmat	http://www.vilber.de/

CONTACT FOR REAGENT AND RESOURCE SHARING

Further information and requests for resources and reagents should be directed to and will be fulfilled by the Lead Contact Lorenza Penengo (penengo@imcr.uzh.ch).

EXPERIMENTAL MODEL AND SUBJECT DETAILS

U2OS shRNF168

Human osteosarcoma U2OS cell line expressing a doxycycline inducible shRNA against RNF168 (kindly provided by J. Lukas) was cultured in DMEM supplemented with 10% FBS, 100 U/mL penicillin, 100 μg/mL streptomycin 1 μg/mL puromycin and 5 μg/mL blasticidin in an atmosphere containing 6% CO_2 at 37°C. shRNA expression was induced by adding doxycycline to the growth media at a final concentration of 1 μg/mL for 96 hr.

U2OS shRNF8

Human osteosarcoma U2OS cell line expressing a doxycycline inducible shRNA against RNF8 (kindly provided by N. Mailand) was cultured in DMEM supplemented with 10% FBS, 100 U/mL penicillin, 100 μg/mL streptomycin 1 μg/mL puromycin and 5 μg/mL blasticidin in an atmosphere containing 6% CO_2 at 37°C. shRNA expression was induced by adding doxycycline to the growth media at a final concentration of 1 μg/mL for 96 hr.

U2OS 53BP1 KO and matching WT U2OS

CRISPR/Cas9 generated 53BP1 KO and the WT U2OS cell line from which they originate (both kindly provided by S. Jackson) were cultured in DMEM supplemented with 10% FBS, 100 U/mL penicillin, and 100 μg/mL streptomycin in an atmosphere containing 6% CO_2 at 37°C.

RIDDLE and RIDDLE HA-RNF168

RIDDLE patient fibroblasts and the same cell line reconstituted with HA-RNF168 (both kindly provided by G. Stewart) were cultured in DMEM supplemented with 10% FBS, 100 U/mL penicillin, and 100 μg/mL streptomycin in an atmosphere containing 6% CO_2 at 37°C.

U2OS

Human osteosarcoma U2OS cells were cultured in DMEM supplemented with 10% FBS, 100 U/mL penicillin, and 100 μg/mL streptomycin in an atmosphere containing 6% CO_2 at 37°C.

AT22IJE-T cell lines

Ataxia-telangiectasia fibroblast cell line AT22IJE-T carrying an empty expression vector (pEBS7) and the same cell line expressing recombinant ATM (YZ5) (kindly provided by Y. Shiloh) were cultured in DMEM supplemented with 20% FBS, 100 U/mL penicillin, and 100 μg/mL streptomycin in an atmosphere containing 6% CO_2 at 37°C.

U2OS Flp-In T-REx cell lines

The four cell lines for the doxycycline inducible expression of wild-type or mutant RNF168 presented in this manuscript (EV, WT^{res}, $R57D^{res}$ and UBD^{res}) were generated by transfecting 160,000 U2OS Flp-In T-REx cells (kindly provided by D. Durocher) with 2 μg of a 9:1 mixture of pOG44 Flp-Recombinase Expression Vector (Thermo Fisher) and the respective expression plasmid. The transfected cells were then cultured in DMEM supplemented with 10% FBS, 100 U/mL penicillin, 100 μg/mL streptomycin, 10 μg/mL hygromycin B and 5 μg/mL blasticidin in an atmosphere containing 6% CO_2 at 37°C for 2 weeks to select for positive transformants. After the selection phase the cell lines were grown in DMEM supplemented with 10% FBS, 100 U/mL penicillin, 100 μg/mL streptomycin, 5 μg/mL hygromycin B and 5 μg/mL blasticidin in an atmosphere containing 6% CO_2 at 37°C. Expression of the respective constructs was induced by adding doxycycline to the growth media at a final concentration of 1 μg/mL for 12 hr (DNA fibers) or 24 hr (immunofluorescence and PLA).

RPE H2AX S139A and matching WT RPE

CRISPR/Cas9 generated H2AX S139A and the WT RPE cell line from which they originate (both kindly provided by S. Jackson) were cultured in DMEM supplemented with 10% FBS, 100 U/mL penicillin, and 100 μg/mL streptomycin in an atmosphere containing 6% CO_2 at 37°C.

U2OS ZRANB3 KO

Human osteosarcoma U2OS ZRANB3 KO cells (kindly provided by D. Cortez) were cultured in DMEM supplemented with 10% FBS, 100 U/mL penicillin, and 100 μg/mL streptomycin in an atmosphere containing 6% CO_2 at 37°C.

METHOD DETAILS

Immunofluorescence

U2OS cells were grown on sterile 12-mm diameter glass coverslip, incubated for 30 min with 10uM EdU, washed with 1X PBS and preextracted for 10 min with CSK-buffer (10 mM PIPES, 50 mM NaCl, 300 mM Sucrose, 3 mM $MgCl_2$, 1 mM EGTA, and 0.5% Triton X-100) on ice, fixed in 4% buffered paraformaldehyde, washed three timea with 1X PBS, permeabilized for 10 min at room temperature in 0.3% Triton X-100 (Sigma-Aldrich) in PBS and washed twice in PBS. EdU detection was performed with a Click-iT Plus EdU Alexa Fluor 647 Imaging Kit according to the manufacturer's recommendations (Thermo Fisher Scientific) before incubation with primary antibodies. All primary and secondary antibodies were diluted in PBS supplemented with 3% BSA. Incubation with primary antibodies was performed at room temperature for 2 hr. Coverslips were washed three times with PBS containing 0.1% Tween-20 (Sigma-Aldrich). Secondary-antibody incubations were performed at room temperature for 1 hr. After one wash with PBS containing 0.1% Tween-20 and one with PBS, coverslips were incubated for 10 min with PBS containing DAPI (0.5 mg/mL) at room temperature to stain DNA. Following three washing steps in PBS, coverslips were briefly washed with distilled water, dried on 3 mm paper and mounted in 5 μL Prolong Gold antifade reagent (Invitrogen).

Confocal microscopy

Imaging was performed with support of the Center for Microscopy and Image Analysis, University of Zurich. Representative IF images were acquired on a Leica SP8 automated upright confocal laser scanning microscope using an HCX PL APO CS2 63x immersion oil objective (NA 1.4). Z series were de-convolved using Huygens Deconvolution software and a representative single Z slice is shown.

Proximity Ligation Assay (PLA)

U2OS cells were grown on sterile 12-mm diameter glass coverslip, incubated for 30 min with 10 μM EdU, washed with cold PBS and pre-extracted in CSK buffer (HEPES-KOH 20 mM pH 7.4, 100 mM NaCl, 3 mM $MgCl_2$, 1 mM EGTA and 0.5% Triton X-100) for 5 min on ice. After one wash with cold PBS, cells were fixed in 4% buffered paraformaldehyde, washed three times with PBS,

permeabilized for 10 min at room temperature in 0.3% Triton X-100 (Sigma-Aldrich) in PBS and washed twice in PBS. EdU detection was performed according to the manufacturer's recommendations (Thermo Fisher Scientific) before incubation with primary antibodies. Coverslips were then incubated with anti-FLAG and anti-PCNA antibody and *in situ* proximity ligation was performed using a Duolink Detection Kit (Sigma-Aldrich).

Quantitative image-based microscopy (QIBC)

Automated multichannel wide-field microscopy for QIBC was performed as described previously (Toledo et al., 2013) on an Olympus ScanR Screening System equipped with wide-field optics, a 20x, 0.75-NA (UPLSAPO 20x), an inverted motorized Olympus IX83 microscope, a motorized stage, IR-laser hardware autofocus, a fast emission filter wheel with single-band emission filters, and a 12-bit digital monochrome Hamamatsu ORCA-FLASH 4.0 V2 sCMOS camera (dynamic range 4,000:1, 2,048 3 2,948 pixel of size 6.5 3 6.5 mm, 12-bit dynamics). Images were acquired in an automated fashion with the ScanR acquisition software (Olympus 2.6.1). Images containing at least 2,000 cells per condition were acquired under non-saturating conditions and identical settings were applied to all samples within one experiment. Images were processed and analyzed with the inbuilt Olympus ScanR Image Analysis Software Version 2.5.1, a dynamic background correction was applied, nuclei segmentation was performed using an integrated intensity-based object detection module using the DAPI signal, and foci segmentation was performed using an integrated spot-detection module. Fluorescence intensities were quantified and are depicted as arbitrary units. These values were then exported and analyzed with Spotfire data visualization software (TIBCO, version 5.0.0). Within one experiment, similar cell numbers were compared for the different conditions. To visualize discrete data in scatterplots (e.g., foci numbers), mild jittering (random displacement of data points along the discrete data axes) was applied to demerge overlapping data points. Representative scatterplots and quantifications of independent experiments, typically containing several thousand cells each, are shown. Statistical analysis was performed in GraphPad Prism7 forMacOSX using paired t test.

Transfections

For siRNA experiments, cells were transfected with the indicated siRNAs for an indicated amount of time using jetPRIME (Polyplus transfection) according to manufacturer's instruction.

siLuc (72 hr 40 nM; 5′-CGUACGCGGAAUACUUCGAUUdTdT-3′);
siRNF168 (72 hr 40 nM: 5′-CGUGGAACUGUGGACGAUAAUUCAAdTdT-3′);
siRAD51 (24 hr 40 nM: 5′-GACUGCCAGGAUAAAGCUUdTdT-3′);
siRECQ1 (72 hr 40 nM: SMART pool against human RECQ1, NM_032941, Dharmacon);
siBRCA1 (72 hr 40 nM: 5′-GGAACCUGUCUCCACAAAGdTdT-3′);
siSmarcal1 (48 hr 40 nM:5′-AAGCAAGGCCCAUCCCAAAdTdT-3′).

Flow cytometric analysis for γH2A.X/EdU/DAPI

All cell lines subjected to this analysis were labeled with 10 μM EdU for 30 min, harvested by standard trypsinization and subsequently fixed for 10 min in 4% formaldehyde/PBS. Cells were then washed twice and blocked over night at 4°C with 1% BSA/PBS, pH 7.4. They were permeabilized the next day with 0.5% saponin/1% BSA/PBS, and stained with primary mouse anti–γH2AX antibody (05-636; EMD Millipore) diluted at 1:1000 in 0.5% saponin/1% BSA/PBS for 2 hr. This was followed by incubation with a Goat anti-mouse Alexa 647 antibody (A-21235, Thermo Fisher) diluted at 1:125 in 0.5% saponin/1% BSA/PBS for 30 min. The incorporated EdU was labeled according to the manufacturer's instructions (Thermo Fisher). Total DNA was stained with 1 μg/mL DAPI dissolved in 1% BSA/PBS, pH 7.4. Samples were measured on an Attune NxT Flow Cytometer (Thermo Fisher) and analyzed using FlowJo software V.10.0.8 (FlowJo, LLC). Statistical analysis was carried out using GraphPad Prism 7.

Replication fork progression by DNA fiber analysis

This protocol is based on Jackson and Pombo, 1998. All cell lines subjected to this analysis were grown asynchronously and labeled with 30 μM of the thymidine analog chlorodeoxyuridine (CldU; Sigma-Aldrich) for 30 min, they were then washed three times with warm PBS and subsequently exposed to 250 μM of 5-iodo-2′-deoxyuridine (IdU) for 30 min. All cells were collected by standard trypsinization and resuspended in cold PBS at 3.5×10^5 cells/mL. The labeled cells were mixed 1:8 with unlabeled cells. 2.5 μL of this cell suspension were then mixed with 7.5 μL of lysis buffer (200 mM Tris-HCl, pH 7.5, 50 mM EDTA, and 0.5% [w/vol] SDS) on a glass slide. After an incubation of 9 min at RT, the slides were tilted at a 45° angle to stretch the DNA fibers onto the slide. The resulting DNA spreads were air-dried, fixed in 3:1 methanol/acetic acid, and stored at 4°C overnight. The DNA fibers were denatured by incubating them in 2.5 M HCl for 1 hr at RT, washed five times with PBS and blocked with 2% BSA in PBST (PBS and Tween 20) for 40 min at RT. The newly replicated CldU and IdU tracks were stained for 2.5 hr at RT using two different anti-BrdU antibodies recognizing CldU (Abcam, ab6326) and IdU (Becton Dickinson, 347580), respectively. After washing five times with PBST (PBS and Tween 20) the slides were stained with Anti-mouse Alexa 488 (Invitrogen, A-11001) and anti-rat Cy3 (Immuno Research, 712-166-1530) secondary antibodies for 1 hr at RT in the dark. The slides were mounted in 30 μL Prolong Gold antifade reagent (Invitrogen). Microscopy was done using an Olympus IX81 microscope with a CCD camera (Hamamatsu). To assess fork progression IdU rack lengths of at least 120 fibers per sample were measured using the line tool in ImageJ64 software. For sister fork symmetry analysis IdU rack lengths of at least 50 sister fork fibers were measured using the line tool in ImageJ64 software. Statistical analysis was carried out using GraphPad Prism 7.

Neutral comet assay

Asynchronously growing U2OS shRNF168 cells were either left uninduced or depleted of RNF168 by adding doxycycline to the growth media at a final concentration of 1 μg/mL for 96 hr. One uninduced sample was treated with 1 μM camptothecin (CPT) for 1 hr and used as a positive control for DNA double-stranded break formation. Cells were collected by standard trypsinization and resuspended in cold PBS at a concentration of 10^6 cells/mL. 20 μL of cell suspension was then mixed with 600 μL of 0.8% w/v Low Melting Point (LMP) agarose (Lonza) in PBS, previously equilibrated to 37°C. 60 μL of the cell-LMP mixture was then spread onto a comet slide (CometAssay Kit, Trevigen). Slides were incubated at 4°C for 20 min to allow solidification of the LMP. They were subsequently put in lysis buffer (CometAssay Lysis Solution, Trevigen) pre-equilibrated to 4°C and refrigerated overnight. The following day, slides were incubated in cold electrophoresis buffer (300 mM sodium acetate, 100 mM Tris, pH 8.3) for 1 hr at 4°C and then subjected to electrophoresis in a comet chamber for 30 min at 21Volt/300mA. After electrophoresis, the slides were rinsed twice in water, fixed in 70% ethanol at 4°C for 20 min and then dried at 37°C. The comets were than stained using SYBR Gold (Thermo Fisher Scientific) diluted at 1:30,000 in Tris-EDTA (10 mM Tris-HCl pH 7.5, 1 mM EDTA) for 30 min in dark. Microscopy was performed on a Leica DM6 B upright digital research microscope equipped with a DFC360 FX Leica camera at 10x magnification. The images were analyzed using the Open Comet plugin (http://www.cometbio.org) for Fiji. At least 105 cells were analyzed per sample. Statistical analysis was carried out using GraphPad Prism 7.

Protein extraction and western blotting

Extracts from all cell lines were prepared in Laemmli sample buffer (4% SDS, 20% glycerol, and 120 mM Tris- HCl, pH 6.8). 40 μg total protein from cell isolates were loaded onto 4%–20% Mini-PROTEAN TGX Precast Protein Gels (BIO RAD). Proteins were separated by electrophoresis at 16 mA followed by transferring the proteins to Immobilon-P membranes (Thermo Fisher Scientific) for 1 hr at 350 mA (4°C) in transfer buffer (25 mM Tris and 192 mM glycine) containing 10% methanol. Before addition of primary antibodies, membranes were blocked for 1 hr in TBS containing 0.1% Tween 20 and 5% milk.

Production of GST-tagged RNF168 and GST pull-down

For the production recombinant GST-tagged human RNF168 (GST-RNF168) protein pGEX-6P2 RNF168 was transformed into BL21(DE3)pLysS competent bacteria. Next morning, cells were grown in 1 L of 2x TY containing 100 μg/mL Ampicillin, 50 μg/mL Chloramphenicol to an OD_{600} = 0.6. Expression of GST-tagged RNF168 was induced by the addition of 0.5 mM IPTG and cells were grown over night at 18°C in a shaker. Next day, bacteria were harvested by centrifugation and pellets were lysed in 50 mM HEPES (pH 7.5), 200 mM NaCl, 1 mM EDTA, 0.1% IPEGAL, 5% Glycerol, 1 mM PMSF, 1x Protease inhibitor cocktail (Sigma; P8349). Subsequently to sonication and clearing of the lysate, GST-RNF168 was purified by incubating cell lysates with 500 μL Glutathione Sepharose (GE Healtcare; 17-0756-01) for 2 hr at 4° on a rotator. Thereafter, Glutathione Sepharose was washed three times in 1x PBS containing 1% Triton X-100, twice with 1x PBS containing 300 mM NaCl and before two washes with and storage in maintaining buffer (50 mM Tris-HCl pH 7.4, 100 mM NaCl, 10% Glycerol, 1 mM EDTA, 1 mM DTT).

HeLa cells were grown to 70% confluency before cell lysis in lysis buffer containing 50 mM HEPES (pH 7.5), 10% Glycerol, 150 mM NaCl, 1% Triton X-100 1 mM EDTA, 1 mM EGTA, 10 mM NEM, 10 mM Sodium Pyruvate, 50 mM Sodium Fluoride, 1 mM PMSF, 1 mM $MgCl_2$, 100 U/mL Benzonase (Sigma, E1014), 1x Protease inhibitor cocktail (Sigma; P8340). Lysates were cleared by centrifugation. For GST pull-down experiments 500 μg of HeLa total cell extract was incubated with either 10 μg Glutathione Sepharose bound GST or GST-tagged RNF168. Samples were analyzed by western blotting by using mouse anti-PCNA antibody (Santa-Cruz; sc-56).

CoIP

2.5×10^6 HeLa cells were transfected with pcDNA3.1 FLAG or pcDNA3.1 FLAG expressing FLAG-tagged human RNF168 using Lipofectamine 2000 (Thermo Fisher, 11668019) following the manufacturer's instructions. After 24 hr, cells were washed once in 1x cold PBS and lysed in lysis buffer indicated in the section above. 500 μg of cleared cell lysate was subjected to immunoprecipitation using 30 μL anti-FLAG M2 Affinity Gel (Sigma; A2220) and samples were incubated for 3 hr at 4°C on a rotator. After four washing steps with lysis buffer, FLAG beads were denatured in 30 μL 1x Laemmli buffer for 5 min at 95°C.

iPOND

HEKT293T cells were treated either with siLuc (samples: mock, Thy and no Click) or siRNF168 as described above. For iPOND experiment, cells were labeled with 10 μM EdU (Life Technologies; A10044) for 13 (siLuc) or 18 min (siRNF168). For the pulse-chase with Thymidine (Thy Chase), EdU-labeled cells were washed twice with 1x PBS followed by incubation in cell culture medium supplemented with 10 μM Thymidine (Sigma-Aldrich; T1895) for 47 min. For the sample treated with 1 μM CPT (Sigma; C9911), cells were labeled with EdU for 7 min followed by CPT treatment for 30 min. Thereafter, cells were fixed in 1% Formaldehyde (Sigma; F1635) for 12 min and quenched with 0.125 M Glycine (AppliChem; 131340.1211) for 5 min. After removal of supernatant, cells were then scraped off in 1x PBS followed by permeabilization in 1x PBS containing 0.25% Triton X-100 (Sigma; T9284). For the Click-IT, cells were washed once in 1x PBS. Cell pellets were resuspended in 1x PBS containing 10 mM Sodium ascorbate (Sigma; A7631), 2 mM $CuSO_4$ (Sigma; 209198) and either 1 μM Biotin azide (Warburg University) or 1 μM DMSO (Sigma; A3672) and incubated at RT for 2 hr on a rotator. Subsequently, cells were washed three times in 1x PBS, lysed in 50 mM Tris-HCl (pH 8), 1% SDS supplemented with cOmplete Protease Inhibitor (Roche) and chromatin was solubilized by sonication using a Bioruptor

(Diagenode). Cell lysates were cleared by centrifugation for 30 min at maximum speed. Cleared lysates were diluted 1:1 in 1x PBS and binding to streptavidin-agarose (Novagen; 69203) was performed over night at 4°C. Next morning, beads were washed once in 1x PBS, once in 1 M NaCl and again twice in 1x PBS before de-crosslinking two times for 15 min in 2x Laemmli-Buffer. Samples were analyzed by western blotting by using the following antibodies: mouse anti-PCNA (Santa-Cruz; sc-56), rabbit anti-H2AX (Abcam; ab11175) and mouse γH2AX (EMD Millipore; 05-636).

Enrichment for mitochondrial DNA

Mitochondrial DNA was enriched using a mitochondrial DNA Isolation Kit (Abnova; KA0895) according to the manufacturer's instructions. Subsequently the DNA was purified and concentrated, using Amicon size-exclusion columns (Amicon ultra 100K membrane, Millipore) and finally resuspended in TE (Tris-EDTA) buffer.

Neutral and denaturing EM analysis of DNA RIs in human cells

The procedure was performed as recently described (Zellweger and Lopes, 2018) and in the same manner for all cellular systems presented in this manuscript. A total of 2.5–5.0 × 10^6 asynchronously growing subconfluent cells were harvested by standard trypsinization and resuspended in 10 mL cold PBS. *In vivo* psoralen cross- linking of the DNA was performed by exposing twice the living cells to 4,5′,8-trimethylpsoralen at a final concentration of 10 μg/mL followed by short (3 min) irradiation pulses with UV 365-nm monochromatic light (UV Stratalinker 1800; Agilent Technologies). The cells were then washed repeatedly with cold PBS and lysed using a cell lysis buffer (1.28 M sucrose, 40 mM Tris-Cl, pH 7.5, 20 mM $MgCl_2$, and 4% Triton X-100). The thus obtained nuclei were then digested using a digestion buffer (800 mM guanidine-HCl, 30 mM Tris-HCl, pH 8.0, 30 mM EDTA, pH 8.0, 5% Tween 20, and 0.5% Triton X-100) supplemented with 1 mg/mL proteinase K at 50°C for 2 hr. A 24:1 Chloroform:Isoamyl alcohol mixture was used to extract genomic DNA by phase separation (centrifugation at 8,000 rpm for 20 min at 4°C). The DNA was then precipitated by addition of equal amount of isopropanol to the aqueous phase, followed by another centrifugation step (8,000 rpm for 10 min at 4°C). The resulting DNA pellet was washed once with 1 mL of 70% ethanol, air-dried at RT, and finally resuspended by incubating it overnight in 200 μL TE (Tris-EDTA) buffer at RT. 12 μg of the extracted genomic DNA was digested for 5 hr at 37°C with 100 U restriction enzyme PvuII high-fidelity. QIAGEN-tip 20 Plasmid Mini Kit columns were used for RI enrichment. The surface tension of the columns was reduced by incubation with QBT buffer (750 mM NaCl, 50 mM MOPS, pH 7.0, 15% isopropanol [v/v], 0.15% Triton X-100 [v/v]), they were then washed three times with washing buffer 1 (1 M NaCl, 10 mM Tris-HCl, pH 8.0) and finally equilibrated using equilibration buffer (300 mM NaCl, 10 mM Tris-HCl, pH 8.0). Next, the digested genomic DNA was applied to the columns followed by washing twice with washing buffer 2 (900 mM NaCl, 10 mM Tris-HCl, pH 7.0). The DNA was then eluted with 0.6 mL elution buffer (1 M NaCl 10 mM Tris-HCl 1.8% caffeine). Subsequently the DNA was purified and concentrated, using Amicon size-exclusion columns (Amicon ultra 100K membrane, Millipore) and finally resuspended in TE (Tris-EDTA) buffer. For native DNA spreading the benzyldimethylalkylammonium chloride (BAC) method was used to spread the DNA on a water surface and then load it on carbon-coated 400-mesh magnetic nickel grids. For denaturing spreading the spreading mix consisted of 1.0 μL formamide, 0.2 μL glyoxal and 1 μL DNA sample (10-50 ng). This mixture was incubated for 10 min at 42°C in a water bath and chilled immediately after on ice. After this denaturation step the mixture was spread by the BAC method onto carbon-coated 400-mesh magnetic nickel grids. After the spreading procedure, the DNA was platinum coated by platinum-carbon rotary shadowing (High Vacuum Evaporator MED 020; Bal-Tec) to make it electron dense. The grids were scanned using a transmission electron microscope (Tecnai G2 Spirit; FEI; LaB6 filament; high tension $\leq$ 120 kV) and pictures were acquired with a side mount charge-coupled device camera (2,600 × 4,000 pixels; Orius 1000; Gatan, Inc.). The images were processed with DigitalMicrograph Version 1.83.842 (Gatan, Inc.) and analyzed using ImageJ64. Graphs were prepared and statistics performed in GraphPad Prism 7 using paired t test where applicable.

Chromosomal breakage and abnormalities by metaphase spreading

Asynchronously and sub-confluent cells were incubated in fresh medium containing 200 ng/mL nocodazole for 16 hr. They were then harvested by standard trypsinization and swollen with 75 mM KCl for 20 min at 37°C. The swollen mitotic cells were fixed using a fixing solution (3:1 methanol:acetic acid). The fixing step was repeated twice and the cells subsequently resuspend in 200–400 μL of fixing solution. The cells were then dropped onto pre-hydrated glass microscopy slides and air-dried overnight. The slides were mounted the following day using VECTASHIELD Antifade Mounting Medium with DAPI (VECTOR Laboratories). Microscopy was performed on a Leica DM6 B upright digital research microscope equipped with a DFC360 FX Leica camera. Images were analyzed using ImageJ64 and visible chromatid breaks/gaps were counted. Statistical analysis was performed in GraphPad Prism7 for MacOSX using paired t test.

Neutral-neutral 2D-gel analysis

Asynchronously growing U2OS shRNF168 cells either left untreated or depleted of RNF168 by adding doxycycline to the growth media (1 μg/mL final concentration, 96 hr) were transfected with an SV40 based plasmid containing 90 TTC repeats using jetPRIME (Polyplus transfection). The cells were harvested 48 hr after transfection and plasmid DNA was extracted using a modified QIAprep Spin Miniprep protocol. The cells were first resuspended in buffer P1 (QIAprep Spin Miniprep kit), lysed with 0.66% SDS and finally incubated with 0.5 mg/mL proteinase K for 1.5 hr at 37°C. The DNA was denatured by 25 mM NaOH for 1 min followed by neutralization with buffer P3 (QIAprep Spin Miniprep kit), and spun for 15 min in a benchtop centrifuge at 18,200 rpm. The resulting

supernatant was processed on miniprep columns (QIAprep Spin Miniprep kit) according to manufacturer's instructions. The thus extracted plasmid intermediates were digested by EcoRI- DpnI-XmnI followed by EtOH precipitation and resuspension in TE buffer. The intermediates were then loaded onto 2D gels. The first dimension was run on a 0.4% agarose gel (50V, 14.5 hr) and the second dimension was run on a 1% agarose gel with EtBr (140V, 9 hr). All gels were blotted onto Bio-Rad Zeta-probe membranes and probed with radioactively labeled SV40 DNA.

Drugs and reagents

Camptothecin was made fresh for every experiment by dissolving in dimethyl sulfoxide (DMSO) to yield a 20 mM stock (7 mg/mL). Olaparib (AZD2281, Ku-0059436; S1060, Selleckchem) was prepared in DMSO to yield a concentration of 20 mM, aliquoted, and stored at −20°C. Mirin (M9948, Sigma-Aldrich) was dissolved in DMSO to produce a 50 mM stock, aliquoted and stored at −80°C. The ATM inhibitor KU-55933 (Sigma-Aldrich) was dissolved in DMSO to yield a stock concentration of 10 mM, aliquoted and stored at −20°C.

Antibodies

The following primary antibodies were used for western blotting: GAPDH (MAB374, Millipore, kindly provided by A. Sartori), B tubulin (sc-9104; Santa Cruz Biotechnology), CHK1 pS345 rabbit (2348; Cell Signaling Technology), CHK1 mouse (sc-8408; Santa Cruz Biotechnology), KAP1 pS824 rabbit (A300-767A; Bethyl Laboratories), KAP1 rabbit (A300-274A; Bethyl Laboratories), phospho-RPA32 (S4/S8) rabbit (A300-245A; Bethyl Laboratories), RPA32 rabbit (A300-244A; Bethyl Laboratories), RAD51 (H-92) rabbit (sc-8349; Santa Cruz Biotechnology), 53BP1 rabbit (ab36823 Abcam) RNF168 rabbit (generated by R. Freire), RNF8 rabbit (generated by R. Freire). RECQ1 rabbit (ABC1428, Sigma-Aldrich, kindly provided by A. Vindigni). Secondary antibodies used for western blotting were anti-rabbit and anti-mouse ECL (GE Healthcare) The following primary antibodies were used for IF and PLA: FLAG rabbit (F7425, Sigma-Aldrich), FLAG mouse (M2 clone, F1804, Sigma-Aldrich), PCNA mouse (P10, sc-56, Santa Cruz Biotechnology), H2AK15Uub mouse (generated and kindly provided by the lab of Z. Zhang Mayo Clinic College of Medicine, Rochester, Minnesota, USA) and γH2AX rabbit (9718, Cell Signaling). Antibodies recognizing human RNF8 and RNF168 were raised in rabbits. To obtain the purified immunogens, the cDNA corresponding to full-length human RNF8 and to the C-terminal part of human RNF168 (amino acids 300-571) were cloned into pET28a (Novagen) vector for expression in *Escherichia coli*. Subsequently, the recombinant immunogens were purified using Ni-NTA (QIAGEN) following the manufacturer's instructions and then used to immunize rabbits. After eight immunizations, serum was obtained and used for western blots.

DATA AND SOFTWARE AVAILABILITY

Raw imaging data have been deposited to Mendeley Data at https://doi.org/10.17632/hkjz8w9c6p.1.

QUANTIFICATION AND STATISTICAL ANALYSIS

For DNA fiber experiments at least 120 IdU tracts were scored per sample for fork progression analysis and at least 50 sister forks for sister fork symmetry analysis. Every experiment was repeated at least twice. The results were analyzed using GraphPad Prism7 for-MacOSX, using Mann-Whitney test. Whiskers: 10th-90th percentile (****$p < 0.0001$; ***$p < 0.001$; ns, non-significant). Flow cytometry data were analyzed using FlowJo software V.10.0.8 (FlowJo, LLC). The intensity values of 500 EdU positive cells per sample were extracted from the raw data and subjected to statistical analysis using GraphPad Prism 7 (****p value < 0.0001; whiskers: 10th–90th percentile) For the neutral comet assay, at least 105 cells were analyzed per sample for Olive- and Tail-moment using the Open Comet plugin (http://www.cometbio.org/) for Fiji. The experiment was repeated 3 times with comparable results. The results were analyzed using GraphPad Prism7 forMacOSX, using Mann-Whitney test. Displayed as scatterplots with mean and SD (****$p < 0.0001$; ns, non-significant). For quantitative image-based microscopy images were processed and analyzed with the inbuilt Olympus ScanR Image Analysis Software Version 2.5.1. Fluorescence intensities were quantified and depicted as arbitrary units. These values were then exported and analyze with Spotfire data visualization software (TIBCO, version 5.0.0). Within one experiment, similar cell numbers were compared for all different conditions. To visualize discrete data in scatterplots (e.g., foci numbers), mild jittering (random displacement of data points along the discrete data axes) was applied to demerge overlapping data points. Representative scatterplots and quantifications of independent experiments, typically containing several thousand cells each, are shown. Every neutral electron microscopy experiment was repeated twice the number of molecules per sample is indicated in the respective figures and the accompanying EM table. The data were depicted as bar plots with GraphPad Prism7 for MacOSX. For denaturing EM analysis, the bubble size from 20 reversed forks was measured using ImageJ64 resulting in a total of 123 bubbles for the regressed arm, 372 for the parental strand and 600 for the two daughter strands. Frequency distributions for all strand types were computed using GraphPad Prism7 for MacOSX and plotted as histograms with a bin width of 30 nucleotides.

Molecular Cell, Volume *71*

Supplemental Information

Histone Ubiquitination by the DNA Damage Response Is Required for Efficient DNA Replication in Unperturbed S Phase

Jonas Andreas Schmid, Matteo Berti, Franziska Walser, Maria Chiara Raso, Fabian Schmid, Jana Krietsch, Henriette Stoy, Katharina Zwicky, Sebastian Ursich, Raimundo Freire, Massimo Lopes, and Lorenza Penengo

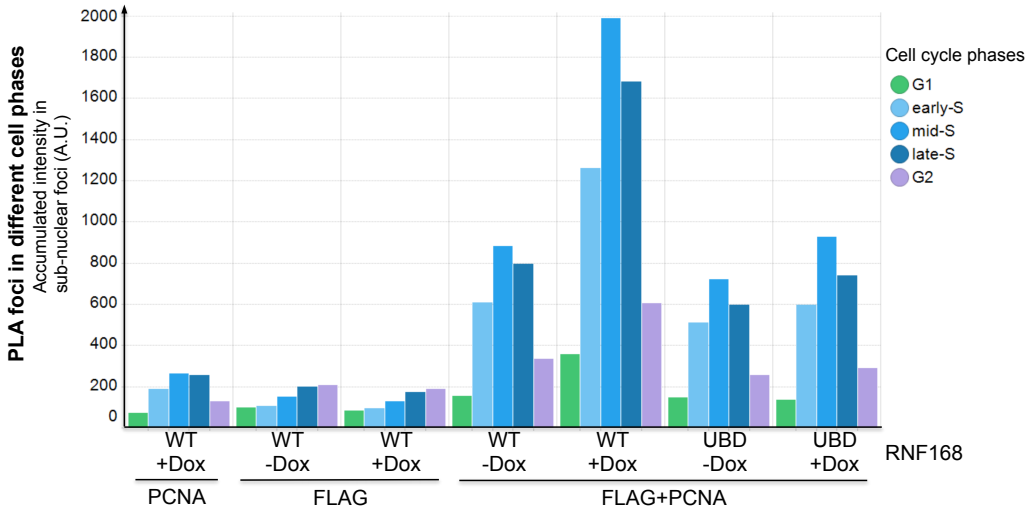

Figure S1. Related to Figure 1
(A) Quantification of PLA *foci* intensity in different cell cycle phases from the experiment described in Figure 1D and 1E.

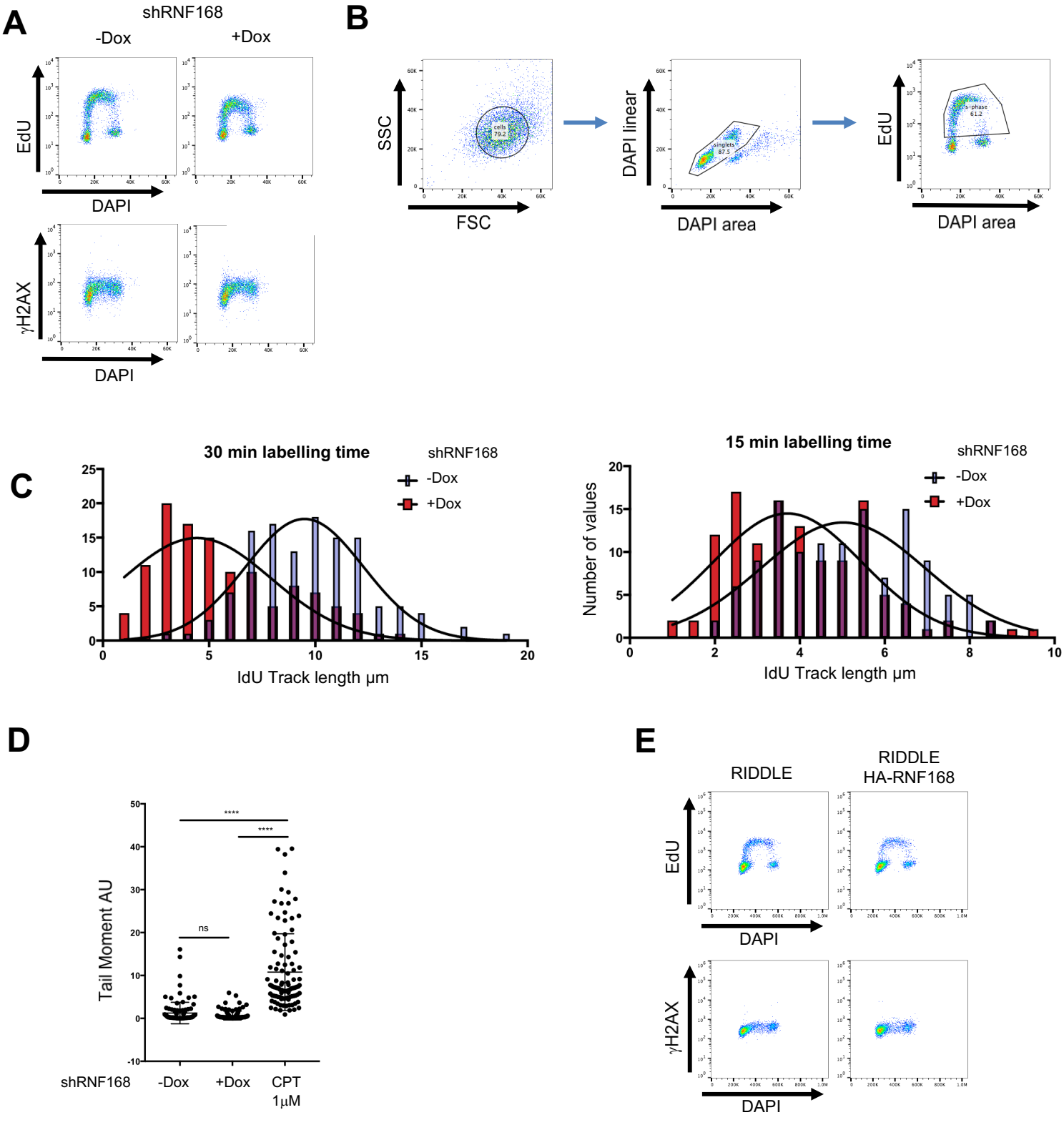

Figure S2. Related to Figure 2

(A) Flow cytometry plots showing the cell cycle distribution and γH2AX intensity profile of control (-Dox) and RNF168 depleted cells (+Dox) from which the intensity values in Figure 2A were extracted. (B) Gating hierarchy used to select S phase cells from which the EdU and γH2AX intensity values were extracted and subjected to statistical analysis in figure 2A. (C) Frequency distributions of fiber lengths in control (-Dox) and RNF168 depleted cells (+Dox) with either 30 min (left) or 15 min (right) labelling time. (D) Quantification of the tail moment in control (-Dox) and RNF168 depleted (+Dox) U2OS shRNF168 cells from a representative neutral comet assay experiment. The olive moments from the same experiment are depicted in Figure 2E. Mean value and standard deviation are indicated as vertical lines for each sample (**** P Value <0.0001). (E) Flow cytometry plots showing the cell cycle distribution and γH2AX intensity profile of RIDDLE patient fibroblasts (RIDDLE) and the same cell line reconstituted with HA-RNF168 (RIDDLE HA-RNF168). The very same cells were used to extract the S phase intensity values depicted in Figure 2F.

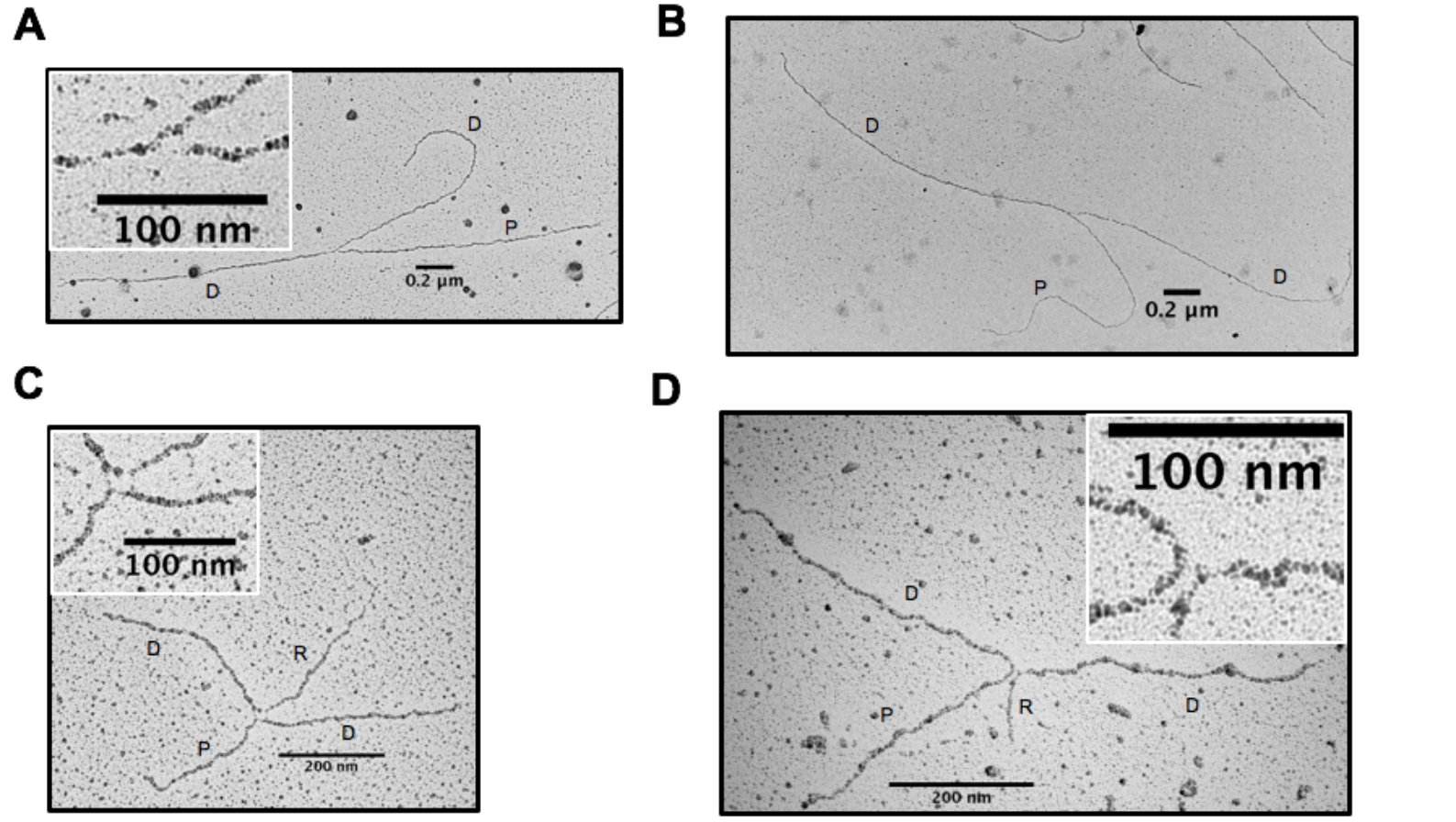

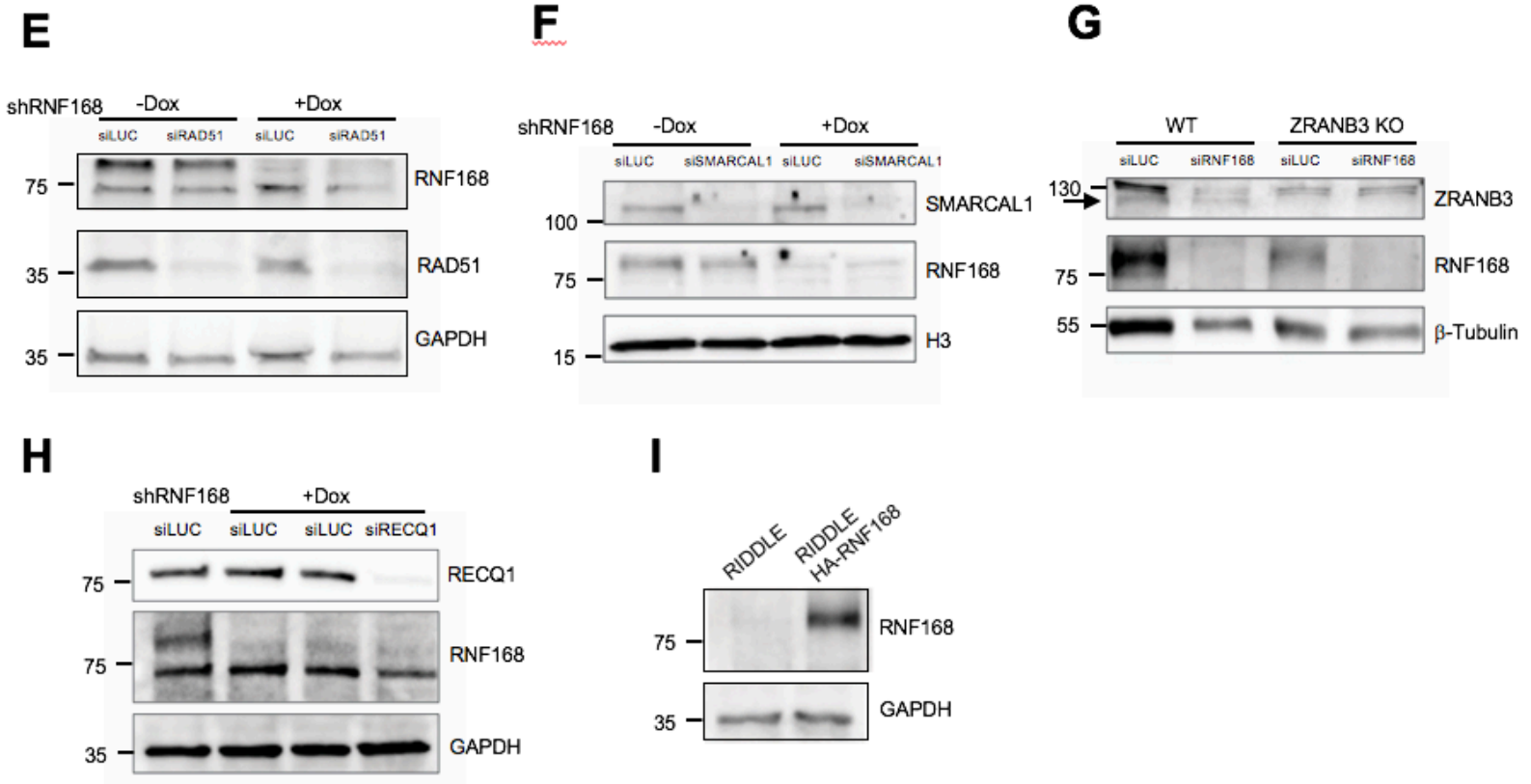

Figure S3. Related to Figure 3
Representative electron micrographs of normal (A and B) and reversed (C and D) replication forks (P: Parental duplex, D: Daughter duplexes, R: Regressed arm). (E) Immunoblot showing the expression levels of RNF168 and RAD51 for the experiment depicted in Figure 3B. (F) Immunoblot showing the expression levels of RNF168 and SMARCAL1 for the experiment depicted in Figure 3C. (G) Immunoblot showing the expression levels of RNF168 and ZRANB3 for the experiment depicted in Figure 3D. The arrow head indicates the band corresponding to ZRANB3. (H) Immunoblot showing the expression levels of RNF168 and RECQ1 for the experiment depicted in Figure 3E. (I) Immunoblot showing the expression levels of RNF168 for the experiment depicted in Figure 3F. GAPDH, histone H3 and ß–tubulin were used as loading controls.

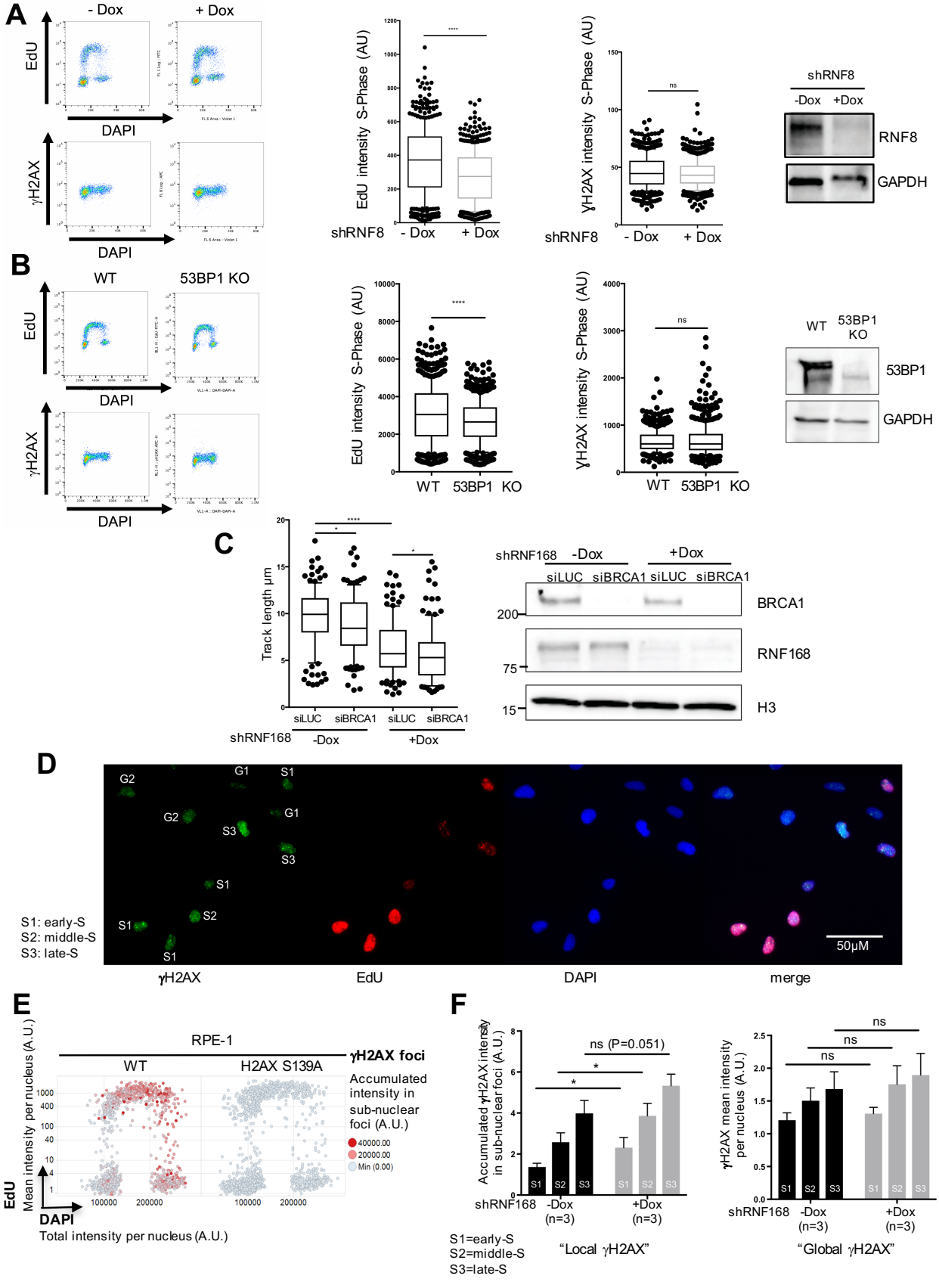

Figure S4. Related to Figure 4

(A) Flow cytometry plots showing the cell cycle distribution and γH2A.X intensity profile of control (-Dox) and RNF8 depleted cells (+Dox). EdU and γH2A.X intensity values of S phase cells were used for statistical analysis in the two panels in the middle. The immunoblot shows the expression level of RNF8 in a representative depletion experiment. (B) Flow cytometry plots showing the cell cycle distribution and γH2A.X intensity profile of CRISPR/Cas9 generated 53BP1 KO cells and the WT U2OS cell line from which they were generated. EdU and γH2A.X intensity values of S phase cells were used for the statistical analysis depicted in the two panels in the middle. The immunoblot shows the expression levels of 53BP1 in WT and 53BP1 KO cells. (C) DNA fiber spreading analysis in control (siLUC, -Dox), BRCA1 depleted (siBRCA1, -Dox), RNF168 depleted (siLUC, +Dox), and BRCA1/RNF168 co-depleted (siBRCA1, +Dox) cells. Protein levels were verified by immunoblot. (D) Representative micrographs from the experiment depicted in Figure 4G showing γH2A.X and EdU levels in different cell cycle phases, after prolonged acquisition time to detect small γH2A.X-positive foci. (E) Representative cell cycle distribution of γH2A.X accumulated intensity in sub-nuclear foci of wildtype (WT) and H2A.X S139A RPE cells as measured by QIBC. (F) Median γH2A.X accumulated intensity in sub-nuclear foci and γH2A.X mean intensity in different sub stages of S-phase from three independent QIBC experiments in control (-Dox, NT) and RNF168 depleted cells (+Dox, NT). (**** P Value <0.0001, * P Value <0.05, Whiskers: 10th–90th percentile).

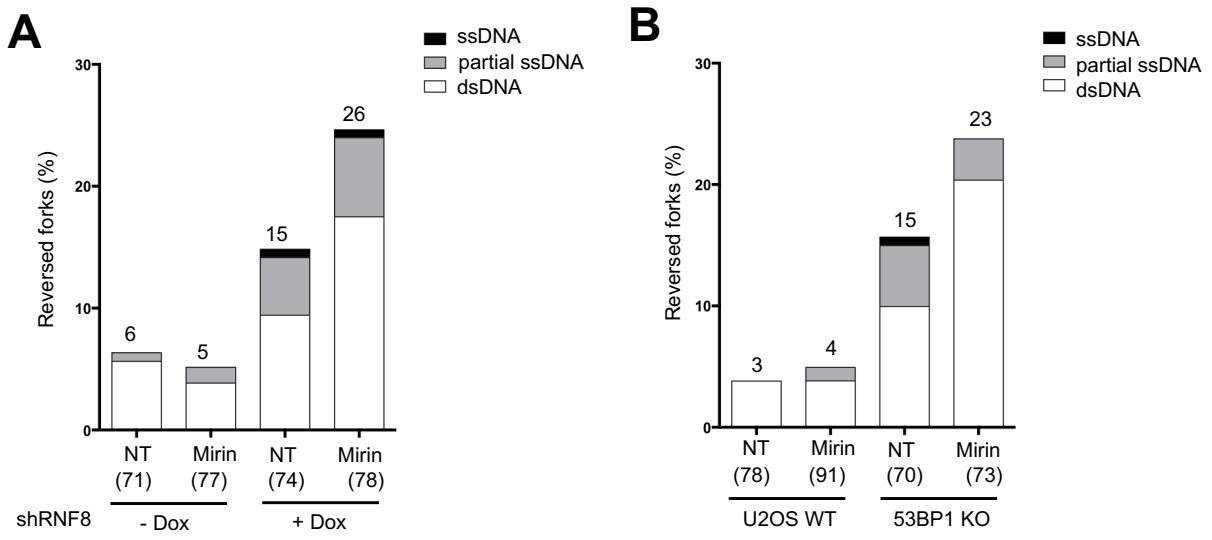

Figure S5. Related to Figure 5

(A) Frequency of reversed replication forks in untreated control cells (NT, -Dox), mirin treated control cells (Mirin, -Dox), cells depleted of RNF8 using an inducible shRNA (NT, -Dox) and RNF8 depleted cells treated with mirin (Mirin, +Dox). The numbers in brackets denote the total of analyzed molecules for each sample. The respective percentage of reversed forks per sample is indicated above each column. The regressed arms of reversed forks have been inspected for singe-stranded DNA stretches. The percentage of partially single stranded regressed arms is indicated in gray and the percentage of completely single-stranded regressed arms in black. (B) Replication fork reversal frequencies in CRISPR/Cas generated 53BP1 KO cells and the WT U2OS cell line from which they were generated. The samples include non-treated WT U2OS cells (NT, U2OS WT), WT cells subjected to mirin treatment (Mirin, U2OS WT), non-treated 53BP1 KO cells (NT, 53BP1 KO) and Mirin treated 53BP1 KO cells (Mirin, 53BP1 KO). Results of additional independent experiments are reported in Table S1B-C.

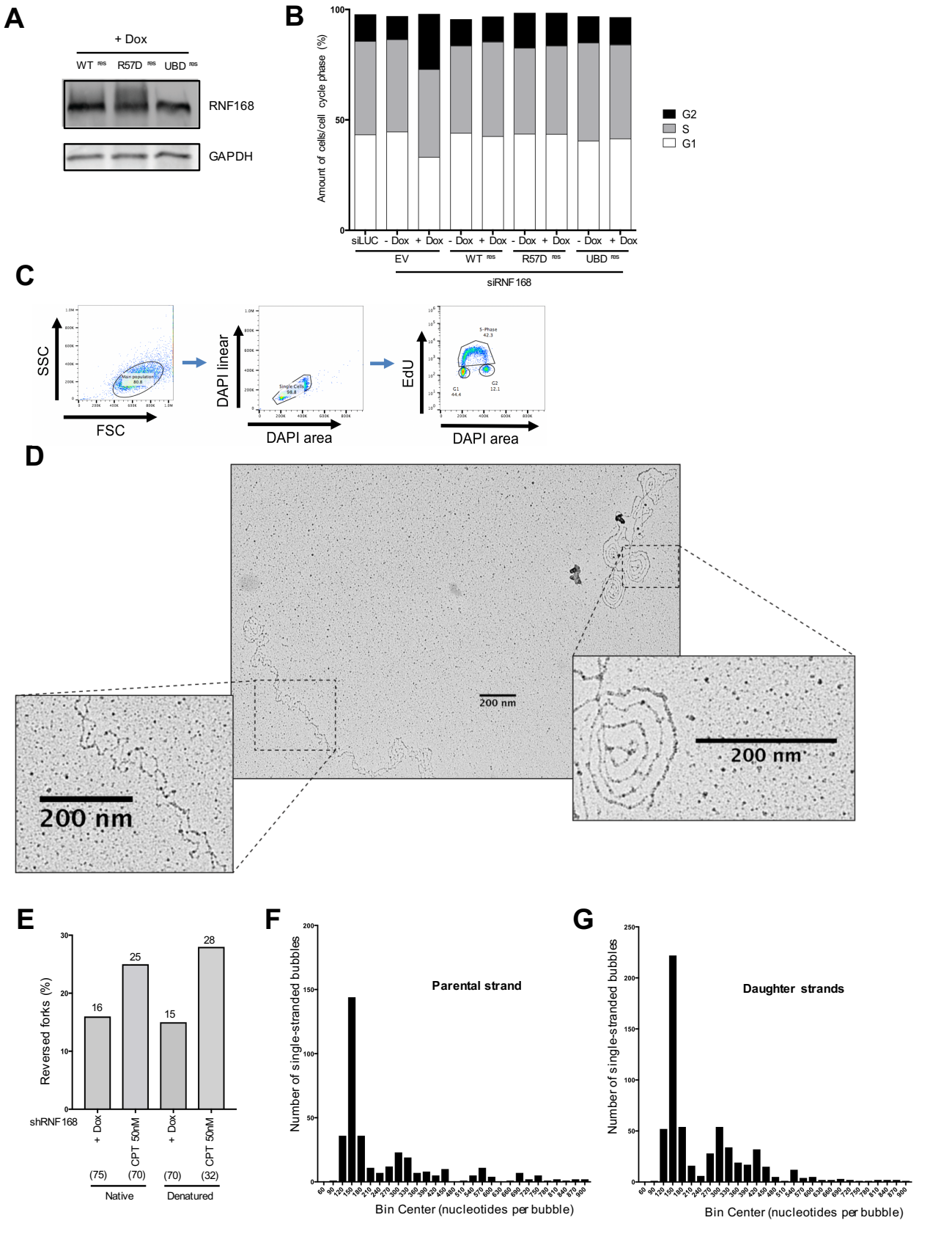

Figure S6. Related to Figure 6.

(A) Immunoblot showing comparable RNF168 expression levels in all three RNF168 expression systems (WT ^{res}, R57D ^{res} and UBD ^{res}) used for the experiment depicted in Figure 6A. (B) Relative cell cycle distribution of the U2OS Flp-In T-REx cell lines used in Figure 6A (EV, WT ^{res}, R57D ^{res} and UBD ^{res}). All four cell lines were depleted of endogenous RNF168 by siRNA. 12h before the experiment the cells were split and either left uninduced (-Dox) or induced by the addition of doxycycline to the growth media (+Dox). U2OS cells carrying an empty vector and transfected with control siRNA (siLUC, EV) were included as a reference. (C) Gating hierarchy used to compute the relative cell cycle distributions depicted in Figure S4B. (D) Representative electron micrograph from a denatured DNA sample enriched for mitochondrial DNA from U2OS cells. The magnified area on the lower left hand side shows the typical bubble structure of genomic DNA, while the double stranded molecule on the top right hand side is of mitochondrial origin. (E) Relative frequency of reversed forks found by native and denaturing transmission electron microscopy in the two samples used to compute the values presented in Figure 6C, S6F and S6G. The respective percentage of reversed forks per sample is indicated above each column. (F) Frequency distribution of the bubble size on the parental strand of denatured reversed replication forks. The same molecules as in Figure 6C were analyzed and plotted as histograms with a bin width of 30 nucleotides. (G) Frequency distribution of the bubble size on the daughter strands of denatured reversed replication forks.

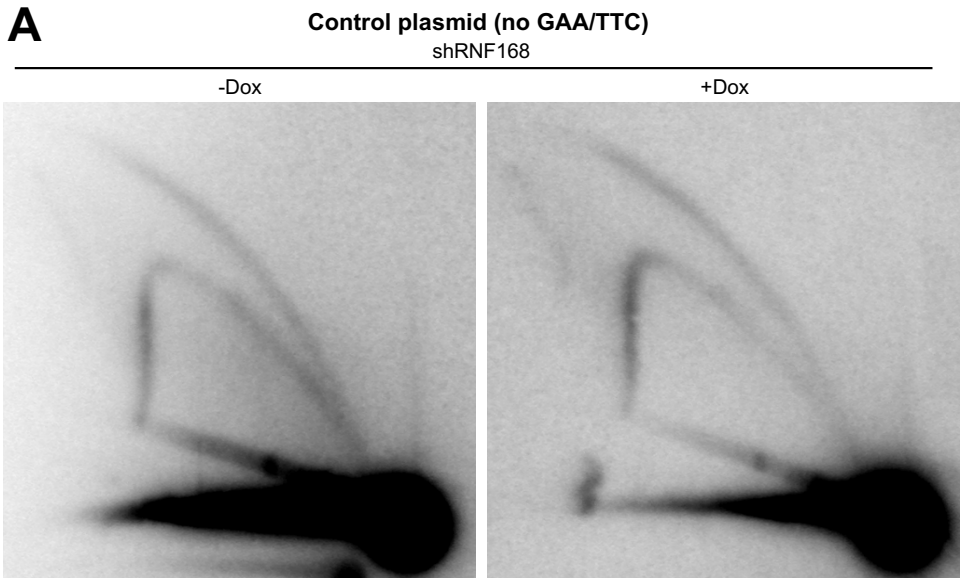

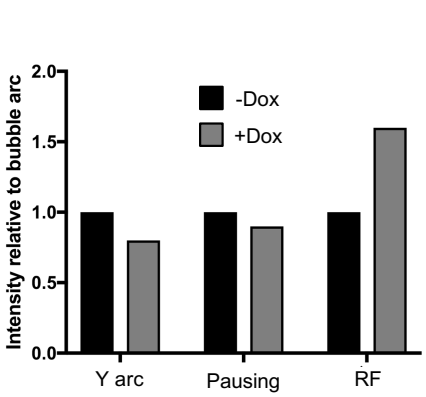

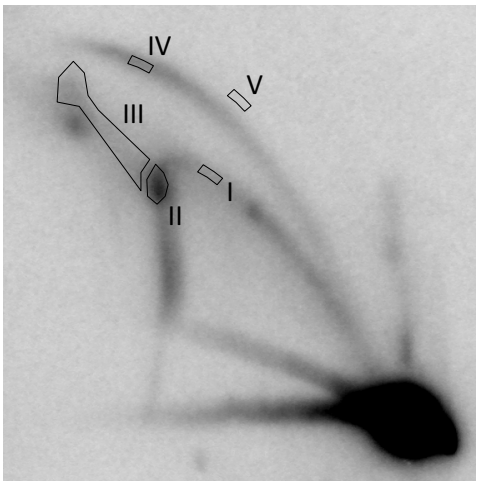

I. Y arc
II. Pausing
III. RF
IV. Bubble arc
V. Background

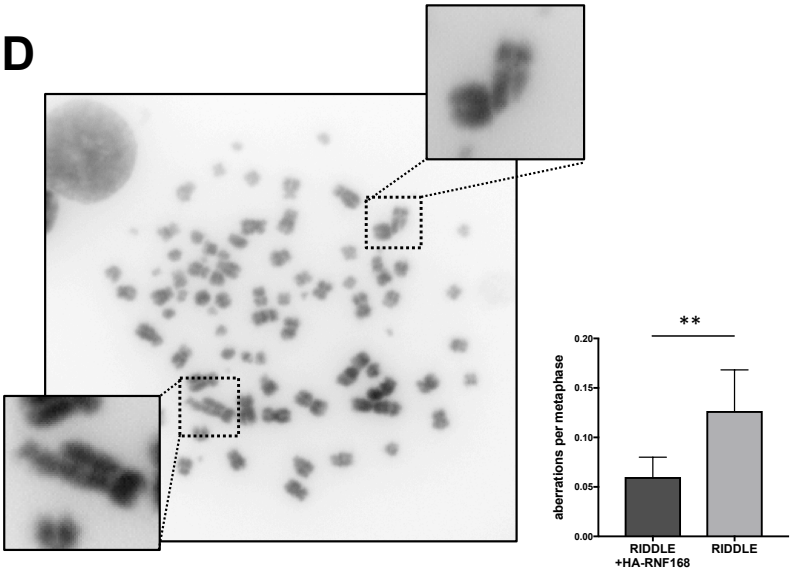

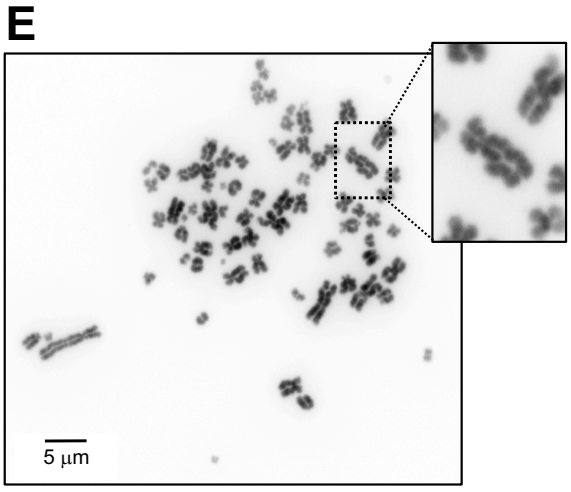

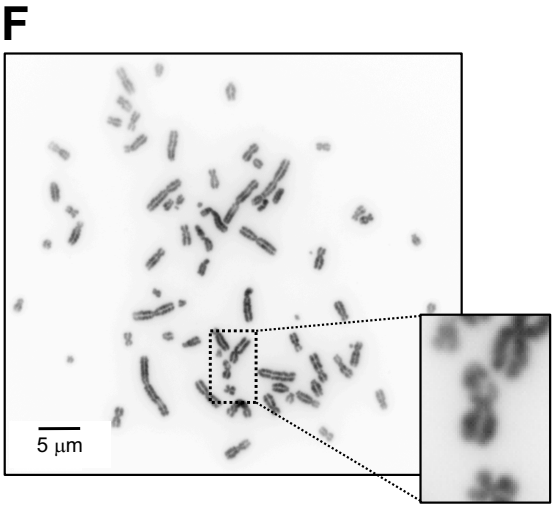

Figure S7. Related to Figure 7.
(A) Typical 2D gel pattern of control plasmid 48 h after transfection into control (-Dox) and RNF168 depleted cells (+Dox). (B) 2D gel pattern with highlighted areas indicating the different regions of the gel that are used for accurate signal quantification. (C) Repetition of the experiment presented in Figure 7A showing comparable results. (D) Number of chromosomal abnormalities observed in RIDDLE patient fibroblasts (RIDDLE) and RIDDLE fibroblasts reconstituted with HA-RNF168 (** P Value <0.01, Paired t test). A representative image is included. (E) and (F) Additional representative images for the metaphase spreads (Figure 7B) to detect chromosomal aberrations in RNF168-depleted U2OS cells.

A

U2OS shRNF168	NT	Mirin	Dox	Dox + Mirin
%RF Exp #1	5 (66)	-	16 (75)	-
%RF Exp #2	4 (73)	5 (72)	15 (73)	32 (74)
%RF Exp #3	5 (75)	6 (70)	15 (73)	29 (82)

B

U2OS shRNF8	NT	Mirin	Dox	Dox + Mirin
%RF Exp #1	5 (85)	-	18 (82)	-
%RF Exp #2	6 (71)	5 (77)	15 (74)	25 (77)
%RF Exp #3	7 (74)	7 (81)	18 (74)	22 (72)

C

U2OS	WT NT	WT Mirin	53BP1Δ NT	53BP1Δ Mirin
%RF Exp #1	4 (78)	5 (91)	16 (70)	24 (74)
%RF Exp #2	6 (92)	5 (80)	15 (71)	22 (74)

D

U2OS	NT	ATMi
%RF Exp #1	5 (86)	17 (75)
%RF Exp #2		21 (82)

E

RPE	WT	H2AX S139A
%RF Exp #1	4 (90)	16 (70)
%RF Exp #2	6 (77)	15 (70)

Table S1. Electron microscopy data for Figures 3-5 and Figure S3 (A-D). **(A)** Percentage of observed reversed forks (% RF) in three independent EM experiments for samples in Figure 3A and Figure 5G. **(B)** Percentage of observed reversed forks (% RF) in three independent EM experiments for samples in Figure 4E (first panel) and Figure S5A. **(C)** Percentage of observed reversed forks (% RF) in two independent EM experiments for samples in Figure 4E (second panel) and Figure S5B. **(D)** Percentage of observed reversed forks (% RF) in two independent EM experiments for samples in Figure 4E (third panel). **(E)** Percentage of observed reversed forks (% RF) in two independent EM experiments for samples in Figure 4L.
Number of analyzed molecules per sample is indicated in brackets.